NATIONAL TECHNICAL UNIVERSITY OF ATHENS

SCHOOL OF NAVAL ARCHITECTURE AND MARINE ENGINEERING

DIVISION OF MARINE ENGINEERING

Diploma Thesis

Dynamic behaviour analysis of fluid film thrust bearings using Computational Fluid Dynamics methods

Koutsoumpas Georgios

Thesis Committee:

Supervisor:	**C. I. Papadopoulos,**	**Associate Professor NTUA**
Members:	**L. Kaiktsis,**	**Professor NTUA**
	G. Papalambrou,	**Assistant Professor NTUA**

Athens, September 2019

ΕΘΝΙΚΟ ΜΕΤΣΟΒΙΟ ΠΟΛΥΤΕΧΝΕΙΟ
ΣΧΟΛΗ ΝΑΥΠΗΓΩΝ ΜΗΧΑΝΟΛΟΓΩΝ ΜΗΧΑΝΙΚΩΝ
ΤΟΜΕΑΣ ΝΑΥΤΙΚΗΣ ΜΗΧΑΝΟΛΟΓΙΑΣ

Διπλωματική Εργασία

Ανάλυση δυναμικής συμπεριφοράς ωστικών εδράνων ολίσθησης με χρήση μεθόδων υπολογιστικής ρευστοδυναμικής

Κουτσούμπας Γεώργιος

Εξεταστική επιτροπή:

Επιβλέπων:	**Χ. Ι. Παπαδόπουλος,**	**Αναπληρωτής Καθηγητής ΕΜΠ**
Μέλη:	**Λ. Καϊκτσής,**	**Καθηγητής ΕΜΠ**
	Γ. Παπαλάμπρου,	**Επίκουρος Καθηγητής ΕΜΠ**

Αθήνα, Σεπτέμβριος 2019

Table of Contents

Acknowledgements

The present work represents the end of my undergraduate studies at the school of Naval Architecture and Marine Engineering which have been a significant milestone of my life and career. It has been a great challenge for me, full of ups and downs, and I am grateful to all the people that have been supporting me in any way throughout this time.

First of all, I would like to thank Associate Professor Christos Papadopoulos. His advice has always been very important and useful to me. Furthermore, I really appreciate that he has provided me with new challenges and helped me extend my limits.

In addition, I wish to thank Anastassis Charitopoulos for dedicating part of his time to assist me through this work and guide me over the difficulties that occurred.

This experience would not have been the same without my fellow classmates. We have been together so much time, sharing so many experiences throughout the course of the studies that I will always think of them when remembering this time. At this point, I also wish to thank all the other friends that have supported me.

Finally, I would like to thank my parents. They have always been there to hear my thoughts and give me their opinions. They have always tried to support me in the best way they could and I really appreciate their efforts.

To all of you, thank you.
Georgios Koutsoumpas

Abstract

In this day and age, the manufacturing industry is constantly seeking to increase its' products efficiency. It is, therefore, imperative to minimise friction losses and a thorough analysis is required for each component. Fluid film thrust bearings have been used extensively to support axial loads between static and rotating parts. Owing to their low cost and reliability, fluid film thrust bearings are used in a variety of applications ranging from high load – low speed marine shafts to high speed – low load turbochargers. Nevertheless, they are being redesigned in order to be more heavily loaded and achieve higher efficiency, resulting in smaller film thicknesses. As a consequence, the risk of bearing failure due to contact between the rotor and the pad under transient loading conditions is increased and a dynamic behaviour analysis should be conducted. To define its' response, the bearing is represented as a single degree of freedom model, and the knowledge of the system's stiffness and damping coefficients is required.

To calculate the aforementioned coefficients, a common method used is to carry out experimental procedures using the specific design. However, the coefficients, in the case of fluid film thrust bearings, are nonlinear resulting in time consuming and expensive experiments for their calculation. Nowadays, the increased available computing power has resulted in advanced computational procedures, which are being investigated to find out an accurate alternative procedure.

In the present work, a computational methodology is proposed to identify the dynamic behaviour of a tapered-land thrust bearing design. A parametric analysis was conducted to optimise the geometry's taper extend and inclination couple. Subsequently, a thermohydrodynamic (THD) computational fluid dynamics (CFD) method is developed the dynamic coefficients of the specific bearing are derived. To conclude, the damping and stiffness coefficients that resulted in the previous step are used in a single degree of freedom model in which a transient load applied to determine the bearing's response.

Σύνοψη

Στη σημερινή εποχή, η κατασκευαστική βιομηχανία επιδιώκει συνεχώς την αύξηση της αποδοτικότητας των προϊόντων της. Είναι, συνεπώς, αναγκαίο να ελαχιστοποιηθούν οι απώλειες λόγω τριβών και είναι απαραίτητη η εκπόνηση ειδικής ανάλυσης για κάθε μέρος. Τα ωστικά έδρανα ολίσθησης έχουν χρησιμοποιηθεί ευρέως για την παραλαβή αξονικών φορτίων μεταξύ σταθερών και περιστρεφόμενων μερών. Το χαμηλό κόστος και η αξιοπιστία των συστημάτων αυτών εξηγούν την χρήση τους σε μεγάλη ποικιλία εφαρμογών που εκτείνονται μεταξύ χαμηλής ταχύτητας περιστροφής αλλά υψηλών φορτίων ναυτικών εφαρμογών και υψηλής ταχύτητας αλλά χαμηλών φορτίων υπερπληρωτών. Εντούτοις, επανασχεδιάζονται ώστε να υπόκεινται σε υψηλότερα επίπεδα φόρτισης για την επίτευξη μεγαλύτερης απόδοσης, με αποτέλεσμα το ελάχιστο πάχος λίπανσης να μειώνεται. Συνεπώς, ο κίνδυνος να προκληθεί επαφή μεταξύ του περιστρεφόμενου και του σταθερού μέρους αυξάνεται καθιστώντας αναγκαία την εκπόνηση μελέτης δυναμικής συμπεριφοράς. Για να προσδιοριστεί η απόκριση του εδράνου, γίνεται αναπαράσταση ως σύστημα ενός βαθμού ελευθερίας, για το οποίο απαιτείται η γνώση των συντελεστών ακαμψίας και απόσβεσης.

Ο υπολογισμός των παραπάνω συντελεστών γίνεται συχνά με τη διεξαγωγή πειραματικών διαδικασιών για την κάθε σχεδίαση. Όμως, στην περίπτωση των ωστικών εδράνων ολίσθησης, οι συντελεστές δεν είναι γραμμικοί και τα πειράματα γίνονται χρονοβόρα και ιδιαίτερα ακριβά. Η αυξημένη υπολογιστική ισχύς που είναι διαθέσιμη σήμερα οδήγησε στην πρόοδο των υπολογιστικών μεθόδων και έδωσε εναλλακτική στα πειράματα.

Στην παρούσα εργασία προτείνεται μία υπολογιστική μεθοδολογία για τον υπολογισμό των δυναμικών συντελεστών ενός ωστικού εδράνου ολίσθησης τύπου tapered-land. Διεξάχθηκε παραμετρική ανάλυση για τον προσδιορισμό του βέλτιστου μεγέθους και κλίσης της ζώνης taper της γεωμετρίας. Ακολούθως, αναπτύχθηκε ένα θερμοϋδροδυναμικό μοντέλο υπολογιστικής ρεστοδυναμικής του συγκεκριμενου εδράνου για τον προσδιορισμό των δυναμικών συντελεστών. Τέλος, οι συντελεστές ακαμψίας και απόσβεσης που προέκυψαν, χρησιμοποιήθηκαν σε ένα μοντέλο ενός βαθμού ελευθερίας στο οποίο εφαρμόστηκε χρονικά μεταβαλλόμενο φορτίο για τον προσδιορισμό της απόκρισης του εδράνου.

Table of figures

List of tables

Nomenclature

c	Damping coefficient [N·s/m]
c_p	Specific heat capacity [J/kg·K]
D	Diameter [m]
F	Friction [N]
h	Film thickness [m]
k	Thermal conductivity [W/m·K]; stiffness coefficient [N/m]
M	Molar mass [kmol/kg]
p	Pressure [Pa]
q	Heat flux [W/m^2]
R	Radius [m]
t	Time [s]
T	Temperature [K]
u/v/w	Velocity in x/y/z direction [m/s]
U	Velocity magnitude [m/s]
W	Load [N]

Greek

μ	Dynamic viscosity [Pa·s]
ν	Kinematic viscosity [m^2/s]
ρ	Density [kg/m^3]
τ	Shear stress [Pa]
φ	Angle [°]
ω	Angular velocity [rad/s]

Non-dimensional

C	Courant number
s	Specific gravity
VI	Viscosity index

1. Introduction

Although efforts to manipulate friction appear in the beginning of human history, systematic studies on the mechanism of friction are relatively recent compared to other fields. Tribology, the science of the relative motion between interactive surfaces, plays a major role in almost any daily application of our lives. Two important concepts in tribology are friction and wear. Various studies have highlighted the cost of friction and wear, showing that even marginal improvements can result in huge differences on the global scale. Depending on the case, the desired relation varies. For instance, brake applications need to minimise wear with constant friction while in bearings both parameters need to be minimised.

Bearings are mechanisms able to carry the load that is transmitted between two bodies that move relatively to one another. Friction between two moving solids contributes to the dissipation of energy, increased wear rates and will eventually lead to the bearing's failure. As a consequence, a means of lubrication is applied to separate the interacting bodies with a layer that will prevent their contact, reducing friction and wear. Lubricant oils are the most common types used but solid and gas lubricants are also used in various applications.

The interaction between the surfaces determines the lubrication type. Hydrodynamic lubrication involves, in general, two relatively moving surfaces, inclined at some angle to create a converging wedge, forming a thin lubricating film. Usually, one surface, called pad, is static, while the other, named runner or rotor moves at a certain speed. Reynolds studied the hydrodynamic lubrication mechanism and derived analytical equations for infinitely long and short bearings which could estimate the load carrying capacity and the generated friction. New designs were introduced, including tapered-land and pocket wedges. The characteristic of hydrodynamic lubrication is that the surfaces are fully separated and is achieved when the runner is moving at a sufficient velocity. If this condition is not met, partial or mixed hydrodynamic lubrication regime occurs. At even lower velocities, as it occurs during engine startup, hydrodynamic lubrication cannot be formed leading to solid contact, which defines boundary lubrication. Apart from hydrodynamic lubrication, in many applications hydrostatic lubrication is used. The main feature is that it is not necessary to have relative motion since the lubricant is fed under pressure by external means. In this case, the film thickness can be controlled by adjusting the pressure. Consequently, it can operate under high loads without any contact issues. Finally, another type of lubrication is the elastohydrodynamic lubrication in which the elastic deformation of the bodies are taken into consideration.

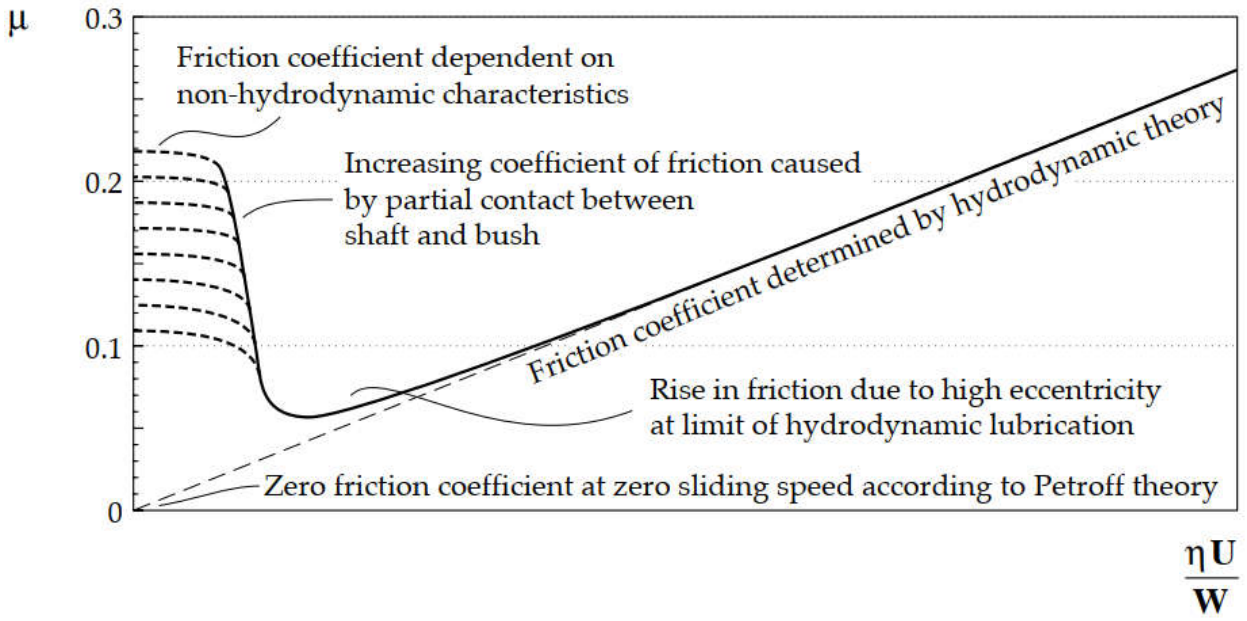

FIGURE 1.1: Friction coefficient changes at the limits of hydrodynamic lubrication [2].

Fluid film journal and thrust bearings operate under the hydrodynamic lubrication principle. Journal bearings are designed to support radial loads and consist of an internal shaft rotating inside a stationary hollow cylinder. On the other hand, thrust bearings support axial loads and are commonly used in marine applications to receive the propeller's thrust.

Reynolds' equations and a plethora of studies conducted focus on the static behaviour of bearings mainly looking for more accurate ways to calculate load and friction values, testing new designs or optimising existing ones. However, in many applications bearings operate under constantly transient conditions meaning that the study of their response is imperative.

Literature review

Due to the complex computations involved in the determination of the dynamic coefficients of a thrust bearing's response, the available literature is quite recent since the rapid increase of the available computational power.

Nevertheless, a study conducted by Eskild Storteig and Maurice White [9] on tapered-land thrust bearings solved the Reynolds' equation using a 1-D finite element technique taking into account hot oil carry-over effect to calculate it's dynamic coefficients. The results showed a relative agreement with coefficients calculated with 2-D methods.

Zhu and Zhang [10] examined the transient axial response of a sector-shaped thrust bearing using a finite difference method to solve the Reynolds' equation. The results highlighted the significance of a nonlinear analysis and that the dynamic coefficients depend strongly on the initial film thickness. .

In [11], Jang and Lee explain that two methods are commonly used to calculate stiffness and damping coefficients. The first, considered as the physical perturbation method, consists in differentiating the forces with respect to finite displacements (for the stiffness coefficient) and finite velocities (for the damping coefficient). Regardless of the method's simplicity, the time necessary for the calculations is significant. The latter is the mathematical perturbation method and uses the finite element method on the perturbed Reynolds' equation. The study continues to calculate the dynamic coefficients of a thrust and journal bearing coupling.

In [12], Srikanth et al. used a finite difference method to solve the Reynolds' equation and calculate the pressure in the oil film of a tilting pad thrust bearing. Variations of the film thickness and the runner's axial velocity allow the calculation of stiffness and damping coefficients.

Papadopoulos et al. [13] proposed a computational method to determine the stiffness and damping coefficients of thrust bearings using Computational Fluid Dynamics. The method acknowledges both translational and tilting motion of the bearing. A hydrodynamic model is set in a steady-state condition (constant rotational speed and minimum film thickness values). Subsequently, a translational or tilting micro-perturbation is forced altering the axial and tilting velocities. The damping coefficient can be calculated by the ratio of the difference of load capacity (for the translational motion) or the average moment (for the tilting motion) and the velocity alteration. Finally, the model is allowed into a new steady-state which allows the calculation of the stiffness coefficient using the minimum film thickness variations instead of the velocity. The proposed method was applied for smooth and textured pad bearing with results that confirmed published data.

Other studies concerning the dynamic response of various types of thrust bearings were conducted. More specifically, in [14], the dynamic coefficients of foil thrust bearings were calculated with CFD tools by imposing a sinusoidal motion to the rotor. The results show agreement with previously published research [15].

Snyder and Brown [16] compared the dynamic coefficients of a simple 2D infinitely long slider derived from Navier-Stokes equations, perturbed and transient Reynolds' equation.

Similar procedures were implemented in [17]-[18], regarding the dynamic coefficient of journal bearings.

A similar approach to that proposed by Papadopoulos was used in [19] by Vieira and Cavalca which solved the Reynolds' equation, instead of the Navier-Stokes equations, to determine the dynamic coefficients for both axial and tilting motions of a tapered-land thrust bearing.

Charitopoulos et al. [20]-[21], developed a CFD thermohydrodynamic model to analyse the operational characteristics of different types of thrust bearings (tapered-land, textured pad, open and closed pocket) and optimise the design. The study examined a set of steady-state conditions (minimum film thickness between 10-80μm, rotational speed between 1-10kRPM) and compared the load capacity, friction torque and maximum temperature on fluid and pad between types. The model was used to optimise automotive turbocharger thrust bearings which operate in a wide range of rotational speeds. In [22], a curved pocket thrust bearing was optimised.

Goals of present study

The main goal of this study is to identify the dynamic behaviour of a tapered-land thrust bearing using the physical perturbation method proposed by Papadopoulos [12], but accounting only for translational motions between pad and rotor.

To achieve this result, the Navier-Stokes equations been solved using the Finite Volume Method. A conjugate heat transfer problem has been simulated that calculated the load and friction forces of a single pad sector for different minimum film thicknesses. The utility has been enhanced with mesh motion capabilities to simulate the axial motion of the rotor. This process created stiffness and damping coefficient maps for the specific geometry.

Ultimately, a single degree of freedom model has been represented using the MATLAB-Simulink environment which used the derived coefficients to predict the response of the bearing under transient load conditions. The results have been evaluated by imposing the resulting displacement history to a transient solver and comparing it with the initial force function used.

2. Lubricants

As mentioned previously, to achieve the hydrodynamic lubrication regime a means of lubrication is necessary to fully separate the two relatively moving surfaces. One of the most common liquid for lubrication is lubricants. At first, mineral only oil lubricants were used, which were derived from the distillation process of crude oil. The properties such lubricant depended mainly on the process used and the source of the crude oil. Mineral oils were cheap, but they displayed some disadvantages which led to the development of semi and fully synthetic oils to deal with issues such as the viscosity drop at high temperatures, oxidation and combustion. Today, semi and fully synthetic oils are common in many applications due to their enhanced properties. However, mineral oils are still used in cases with low requirements.

Viscosity

The great variety of lubricants means that careful consideration is required when evaluating the lubricant selection in any case should. Viscosity is probably the most important property when considering type of oil. To define viscosity two parallel plaques separated by a fluid are considered. The proportionality coefficient between the shear stress generated when trying to move one surface and the velocity gradient across the fluid is the dynamic viscosity μ:

$$\mu = \tau \frac{\partial u}{\partial y} \tag{1}$$

Common units used for the dynamic viscosity are Pa · s and cP.

The kinematic viscosity ν, on the other hand, is defined as the ratio of the dynamic viscosity and the fluid's density:

$$\nu = \frac{\mu}{\rho} \tag{2}$$

It is usually measured in cSt or m^2/s.

Viscosity is highly affected by temperature. The American Society for Testing Materials (ASTM) developed an empirical chart based on Walther's equation for the viscosity-temperature relationship, which is:

$$\log_{10} \log_{10}(\nu + b) = a - c \log_{10} T \tag{3}$$

Where:

ν	is the kinematic viscosity [cSt];
T	is the temperature [K];

b is a constant which ranges between 0.6 and 0.7.

Depending on the case, *b* is set arbitrarily. Consequently, the knowledge of the kinematic viscosity of an oil at two temperatures defines parameters *a* and *c*, allowing the calculation of the viscosity at any other temperature. Fig. 2.1, below, displays the interpolation done by the ASTM equation for an ISO-VG46 oil.

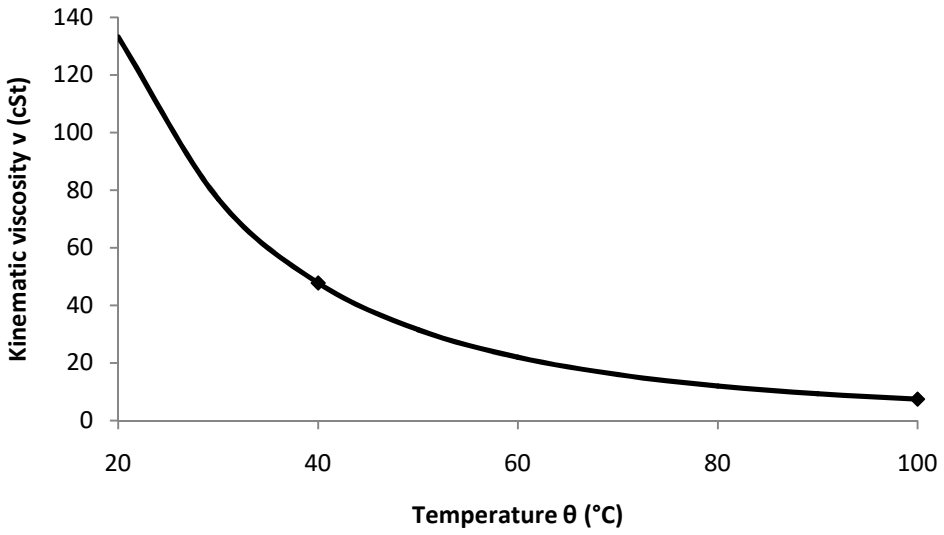

FIGURE 2.1: Kinematic viscosity - Temperature relation (ASTM equation).

For applications that operate in variable temperature conditions the temperature sensitivity of viscosity is extremely important. This feature is measured using the viscosity index (VI). This index is used to compare the oil with two reference oils that display a significantly different behaviour in temperature sensitivity. Oils with high VI are less affected by temperature changes than oils with low VI. Historically, paraffinic mineral oils originating from Pennsylvania had excellent temperature behaviour and were given VI value of 100. On the other hand, Texan mineral oils displayed great viscosity difference when the temperature was altered and they were given VI value of 0. The index for an oil of interest is calculated using the following formula:

$$VI = \frac{L - U}{L - H} \cdot 100 \qquad (4)$$

Where:

L is the viscosity of VI=0 oil at 40°C;

H is the viscosity of VI=100 oil at 40°C;

U is the viscosity of oil of interest at 40°C.

Values for H and U can be found in literature. Owing to the introduction of new generation synthetic oils, the scale is extended also above VI=100. In that case, the following formula is used:

$$VI = 100 + \frac{10^N - 1}{0.00715} \quad (5)$$

Where:

N is a constant equal to: $N = \frac{\log H - \log U}{\log V}$;

V is the viscosity of oil of interest at 100°C (V>2cSt).

Viscosity is also dependant on pressure and it increases with pressure. For pressures below 0.5GPa, the Barus equation can be used:

$$\mu_p = \mu_0 e^{\alpha p} \quad (6)$$

Where:

$\mu_{p/0}$ is the dynamic viscosity at pressure p/ambient [Pa·s];

α is the slope of the natural logarithm of dynamic viscosity versus pressure.

The Reynolds' analysis, mentioned previously, was based on the assumption that the lubricant is Newtonian, which is generally true for mineral oils. Newtonian oils are characterized by a constant slope between shear stress and shear rate, which means that the viscosity is constant. Other oil types, however, can have different behaviour. For instance, multigrade oils suffer from the reduction of viscosity in high shear strain conditions, phenomenon known as shear thinning, in this cases caused by the alignment of the long polymer molecules added to the oil.

Specific heat capacity

Specific heat capacity is a thermophysical property that expresses the amount of heat necessary to raise one unit temperature per unit mass.

$$C_p = \frac{Q}{m \cdot \Delta T} \quad (7)$$

The value varies linearly with temperature and can be approximated from equation:

$$C_p = \frac{1.63 + 0.0034(T - 273.15)}{\sqrt{s}} \quad (8)$$

Where,

C_p is the specific heat capacity [kJ/kg·K];

T is the temperature [K];

s is the oil's specific gravity at 15.6°C.

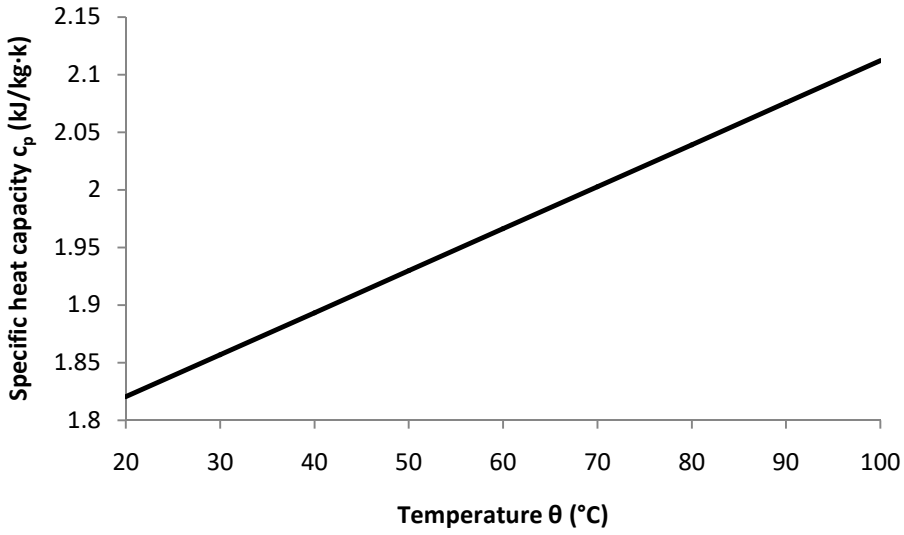

FIGURE 2.2: Specific heat capacity - temperature equation.

Thermal conductivity

Thermal conductivity describes the ability to conduct heat and is the coefficient *k* represented in Fourier's law of conduction:

$$q = -k\frac{dT}{dx} \quad (9)$$

It is also a temperature-dependent thermophysical property which can be approximated from equation:

$$k = \frac{0.012}{s} \cdot \left(1 - \frac{1.667 \cdot (T - 273.15)}{10^4}\right) \quad (10)$$

Where,

k is the thermal conductivity [W/m·K].

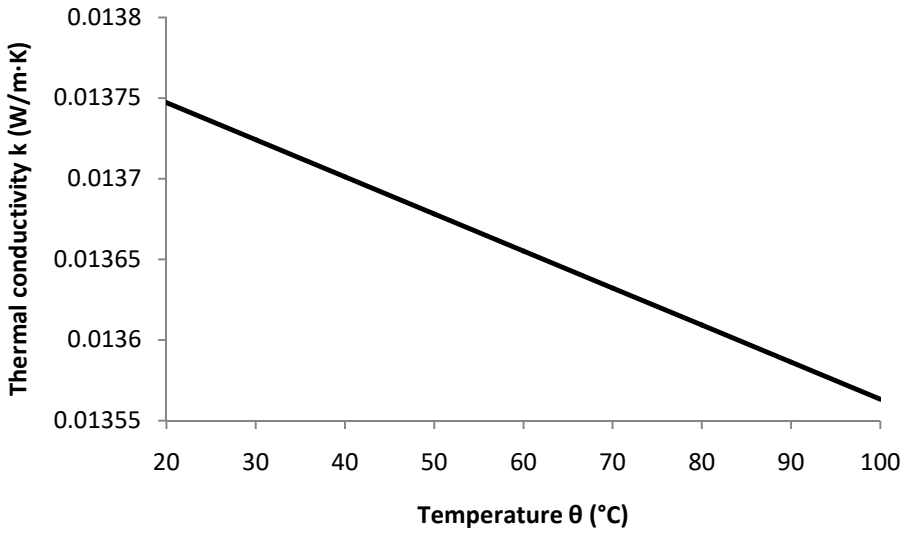

FIGURE 2.3: Thermal conductivity - temperature equation.

Other properties

When considering the selection of the proper oil to use, other properties are also taken into account. In case that low temperatures are expected pour point temperature, which is the lowest temperature that the oil can flow, is evaluated. The cloud point, the temperature at which precipitations of wax appear, may also be considered. Moreover, neutralisation properties may be desired. These are measured with the Total Base Number (TBN) and the Total Acid Number (TAN) for alkaline and acidic oils respectively. The neutralisation number expresses the quantity of KOH to neutralise alkaline or basic compounds. Finally, other less significant properties considered may be the thermal and oxidisation stability and the volatility of the oil.

Cavitation

Considering a phase diagram, it can be noticed that liquid-vapour transition may take place either by changing the temperature or the pressure. The phenomenon that results in the vapour cavity formation from a liquid fluid through pressure decrease is called cavitation. This happens locally, in places that the pressure reaches the vapour pressure. The growth and collapse of the bubbles is usually represented by the Rayleight-Plesset model:

$$\frac{d^2R}{dt^2} + \frac{3}{2R}\left(\frac{dR}{dt}\right)^2 + \frac{1}{\rho R}(p_v - p_0) = 0 \qquad (11)$$

The equation describes the bubble radius R change over time t depending on the cavity pressure p_v and the pressure at infinity p_0 of the fluid with density ρ. The model results in infinite values of pressure and velocity at the moment of bubble destruction.

3. Finite Volume Method

The fundamental physical principles that form the basis of fluid dynamics are:

- The conservation of mass,
- Newton's 2nd law, and
- The conservation of energy.

The equations that describe the fluid flow can be written in different ways depending on the point of view of the observer. The theory of fluid mechanics introduces a finite control volume upon which the equations are developed. This control volume may either be fixed in space, or it may be moving with flow but containing the same particles. The first forms the Eulerian description and leads to a conservative equation form, while the second represents the Lagrangian description and results in non-conservative equations. The derived system is formed of nonlinear partial derivative equations that change in the time and the three dimensional space domain. In addition, the space that the solution is required is usually complex, meaning that an analytical solution is impossible. Advances in the technological field have allowed fast numerical calculations which aided the development of computer simulations as a scientific tool. The method known as Finite Volume Method is usually applied to solve these equations in fluid domains and is based on the Eulerian description, therefore conservative forms are preferred. When the control volumes are finite, the resulting equations are in integral form, while infinitesimally small control volumes lead to the differential form. Thus, the differential form of the flow equations is commonly used.

Continuity equation

The conservation of mass is expressed by the *continuity equation*. It states that the net mass flow that leaves the control volume from its' boundary surface equals the time rate of decrease of mass inside. For a compressible fluid, it can be written in vector notation as:

$$\frac{\partial \rho}{\partial t} + \nabla \cdot (\rho \vec{\boldsymbol{u}}) = 0 \qquad (12)$$

However, oils are incompressible fluids therefore the first term can be neglected leading to:

$$\nabla \cdot \vec{\boldsymbol{u}} = 0 \Longrightarrow \frac{\partial u}{\partial x} + \frac{\partial v}{\partial y} + \frac{\partial w}{\partial z} = 0 \qquad (13)$$

Momentum conservation equations

The equation that results from the second principle is the *momentum equation*, which in Cartesian coordinates is:

$$\frac{\partial(\rho u)}{\partial t} + \nabla \cdot (\rho u \vec{\boldsymbol{u}}) = -\frac{\partial p}{\partial x} + \frac{\partial \tau_{xx}}{\partial x} + \frac{\partial \tau_{yx}}{\partial y} + \frac{\partial \tau_{zx}}{\partial z} + \rho f_x \qquad (14a)$$

$$\frac{\partial(\rho v)}{\partial t} + \nabla \cdot (\rho v \vec{\boldsymbol{u}}) = -\frac{\partial p}{\partial y} + \frac{\partial \tau_{xy}}{\partial x} + \frac{\partial \tau_{yy}}{\partial y} + \frac{\partial \tau_{zy}}{\partial z} + \rho f_y \qquad (14b)$$

$$\frac{\partial(\rho w)}{\partial t} + \nabla \cdot (\rho w \vec{\boldsymbol{u}}) = -\frac{\partial p}{\partial z} + \frac{\partial \tau_{xz}}{\partial x} + \frac{\partial \tau_{yz}}{\partial y} + \frac{\partial \tau_{zz}}{\partial z} + \rho f_z \qquad (14c)$$

In which, p denotes the pressure, f is the body force per unit mass and τ_{ij} denotes a stress in the j-direction acting on a plane perpendicular to the i-axis.

The above equations, however, contain the stress tensor τ which is not known beforehand. Therefore, the introduction of further equations, that relate the normal and shear stresses with the flow, is mandatory. Newton noted that for many materials, including oils, viscous stresses are proportional to the strain rates, hence velocity gradients. Fluids that obey this law are called Newtonian and the stress tensor can be written as:

$$\tau = \begin{bmatrix} \tau_{xx} & \tau_{xy} & \tau_{xz} \\ \tau_{yx} & \tau_{yy} & \tau_{yz} \\ \tau_{zx} & \tau_{zy} & \tau_{zz} \end{bmatrix} = \begin{bmatrix} \lambda(\nabla \cdot \vec{\boldsymbol{u}}) + 2\mu \frac{\partial u}{\partial x} & \mu\left[\frac{\partial v}{\partial x} + \frac{\partial u}{\partial y}\right] & \mu\left[\frac{\partial u}{\partial z} + \frac{\partial w}{\partial x}\right] \\ \mu\left[\frac{\partial v}{\partial x} + \frac{\partial u}{\partial y}\right] & \lambda(\nabla \cdot \vec{\boldsymbol{u}}) + 2\mu \frac{\partial v}{\partial y} & \mu\left[\frac{\partial w}{\partial y} + \frac{\partial v}{\partial z}\right] \\ \mu\left[\frac{\partial u}{\partial z} + \frac{\partial w}{\partial x}\right] & \mu\left[\frac{\partial w}{\partial y} + \frac{\partial v}{\partial z}\right] & \lambda(\nabla \cdot \vec{\boldsymbol{u}}) + 2\mu \frac{\partial w}{\partial z} \end{bmatrix} \qquad (15)$$

Where:

μ is the molecular viscosity;

λ is the second viscosity coefficient $\lambda = -\frac{2}{3}\mu$.

Energy conservation equation

The energy conservation is expressed through the *energy equation,* which states that the rate of energy change in the element is equal to the net flux heat and the rate of work done, and in total energy terms is:

$$\frac{\partial}{\partial t}\left[\rho\left(\frac{1}{2}u^2 + e\right)\right] + \nabla\left[\rho \vec{\boldsymbol{u}}\left(\frac{1}{2}u^2 + e\right)\right] = \rho \vec{\boldsymbol{f}} \cdot \vec{\boldsymbol{u}} - \nabla(p \cdot \vec{\boldsymbol{u}}) + \nabla(\vec{\boldsymbol{\tau}} \cdot \vec{\boldsymbol{u}}) - \nabla(\mathrm{k} \cdot \nabla T) + \rho \cdot q \qquad (16)$$

Where,

e is the internal energy per unit mass;

q is the volumetric heat addition per unit mass;

k is the thermal conductivity.

Discretisation

As mentioned previously, the solution to these equations is sought using numerical methods. The idea behind numerical solutions is to substitute the continuous field with a discrete. Due to the complex shapes that fluid domains usually have, the Finite Volume Method is usually preferred and any shape element can be used as those that appear in Fig. 3.1, below. The differential equations are replaced with algebraic over finite volumes representing the field transforming them into matrix form $\mathbf{M} \cdot U = B$, which can then be solved.

The comprehend the way that the partial differential equations are transformed into matrix form, a general transport equation for a scalar quantity φ is considered, as follows:

$$\int_{V_p} \frac{\partial(\rho\varphi)}{\partial t} dV + \int_{V_p} \nabla \cdot (\rho \vec{\boldsymbol{u}} \varphi) dV - \int_{V_p} \nabla \cdot (\Gamma^{\varphi} \nabla \varphi) dV = \int_{V_p} S_{\varphi}(\varphi) dV \qquad (17)$$

The term $\int_{V_p} \frac{\partial(\rho\varphi)}{\partial t} dV$ represents the *temporal derivative* and is present only in transient conditions. The *convective term* $\int_{V_p} \nabla \cdot (\rho \vec{\boldsymbol{u}} \varphi) dV$ expresses the transportation of the quantity φ due to the velocity field generated by u, while the *diffusion term* $\int_{V_p} \nabla \cdot (\Gamma^{\varphi} \nabla \varphi) dV$ expresses the transportation of φ owing to a concentration differential and the diffusion coefficient Γ_{φ}. Finally, the integral on the right hand side of the equation defines the presence of sources (*source term*).

The first step in the method consists in the discretisation of the domain of interest in a finite number of control volumes. These elements can be of various types of shapes.

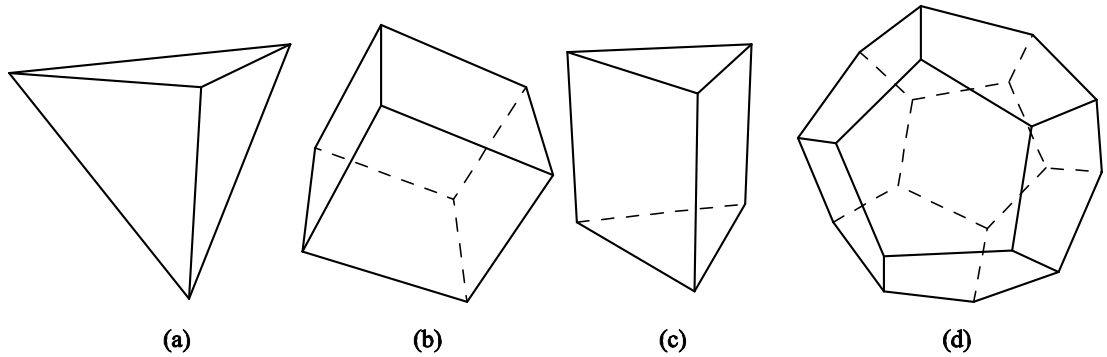

FIGURE 3.1: Types of spatial discretisation, (a) Tetrahedron, (b) Hexahedron, (c) Prism, (d) Polyhedron.

For every control volume V_P the following details are stored:

- The location of the centroid **P** calculated from $\int_{V_P}(x - x_P)dV = 0$,
- The vectors **d** connecting P with the centroids of the neighbouring control volumes,
- The centre **f** of each face $\mathbf{S_f}$ calculated from $\int_{S_f}(x - x_f)dS = 0$ and the location that **d** intersects the face, and
- The vectors $\mathbf{P_f}$ connecting **P** and each face.

Variables may be stored either on vertices or the cell centres. Cell-centred arrangements are most common. The Taylor series expansion is used to calculate variations inside the cell. Cell-centred arrangements are generally preferred due to their higher accuracy and their mesh generation simplicity.

Using the Divergence (Gauss) theorem, the volume integrals of the convective and diffusion terms are transformed into surface integrals:

$$convection: \quad \int_{V_P} \nabla \cdot (\rho\vec{\boldsymbol{u}}\varphi)dV = \oint_{\partial V_P} d\vec{\boldsymbol{S}} \cdot (\rho\vec{\boldsymbol{u}}\varphi) \tag{18a}$$

$$diffusion: \quad \int_{V_P} \nabla \cdot (\Gamma^{\varphi}\nabla\varphi) = \oint_{\partial V_P} d\boldsymbol{S} \cdot (\Gamma^{\varphi}\nabla\varphi) \tag{18b}$$

According to the theorem, the volume integrals of the divergence are equal to the outward flux through a closed surface. $d\vec{\boldsymbol{S}}$ denotes the normal vector of the face **f** pointing outwards. Subsequently, the surface integrals are converted into a series of summations. Firstly, the integral over the entire element's surface is split into the sum of the integrals over each face. Finally, the integral over each face is approximated using the value at the face centre. This is written as:

$$\oint_{\partial V_P} d\vec{\boldsymbol{S}} \cdot (\rho\boldsymbol{u}\varphi) = \sum_{f}^{faces(V_P)} \int_f d\vec{\boldsymbol{S}} \cdot (\rho\vec{\boldsymbol{u}}\varphi)_f \approx \sum_{f}^{faces(V_P)} \overrightarrow{\boldsymbol{S_f}} \cdot (\rho\vec{\boldsymbol{u}}\varphi)_f \tag{19a}$$

$$\oint_{\partial V_P} d\vec{\boldsymbol{S}} \cdot (\Gamma^{\varphi}\nabla\varphi) = \sum_{f}^{faces(V_P)} \int_f d\vec{\boldsymbol{S}} \cdot (\Gamma^{\varphi}\nabla\varphi)_f \approx \sum_{f}^{faces(V_P)} \overrightarrow{\boldsymbol{S_f}} \cdot (\Gamma^{\varphi}\nabla\varphi)_f \tag{19b}$$

The diffusion term leads to the necessity to calculate gradient terms $\nabla\varphi$. These appear in the momentum equation as pressure derivatives, in turbulence models or even in non-Newtonian viscosity models. A commonly used method is the Green-Gauss Gradient which defines:

$$\nabla\varphi_P = \frac{1}{V_P}\sum_f \overrightarrow{S_f}\varphi_f \qquad (20)$$

Both convection and diffusion terms require face values to calculate the integrals. As stated previously, cell-centred arrangements store the information at the centroid. Consequently, the values at the faces have to be interpolated.

Convective terms interpolation

Central difference scheme

This scheme executes linear interpolation to calculate the flux at the face. Supposing that face **f** connect two adjacent control volumes with centroids **P** and **N**. The value at the face is:

$$\varphi_f = f_x\varphi_P + (1 - f_x)\varphi_N \qquad (21)$$

Where, $f_x = \frac{|x_f - x_N|}{|\overrightarrow{PN}|}$

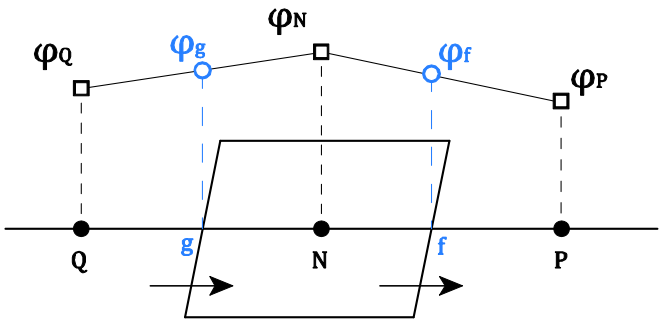

FIGURE 3.2: Central difference scheme.

Since the scheme considers that the variation between the cell centroids is linear and the variation across the cell is also linear in the Finite Volume Method, the scheme is second order accurate. This scheme derives from the Taylor series, neglecting terms of second or higher order. However, its' solutions may be unbounded which means that oscillations may appear in the field solution. The analytical solution of a typical steady-state problem show that at high negative values of Pe_L (Péclet number) the solution tends asymptotically to 1, while at high positive values approaches 0 asymptotically. As shown in Fig. 3.3, numerical results, on the other hand, do not follow the same behaviour. The Péclet number expresses the ratio between advective to diffusive transport. Consequently, this scheme is more suitable in cases with significant diffusion terms since it considers equally upwind and downwind nodes.

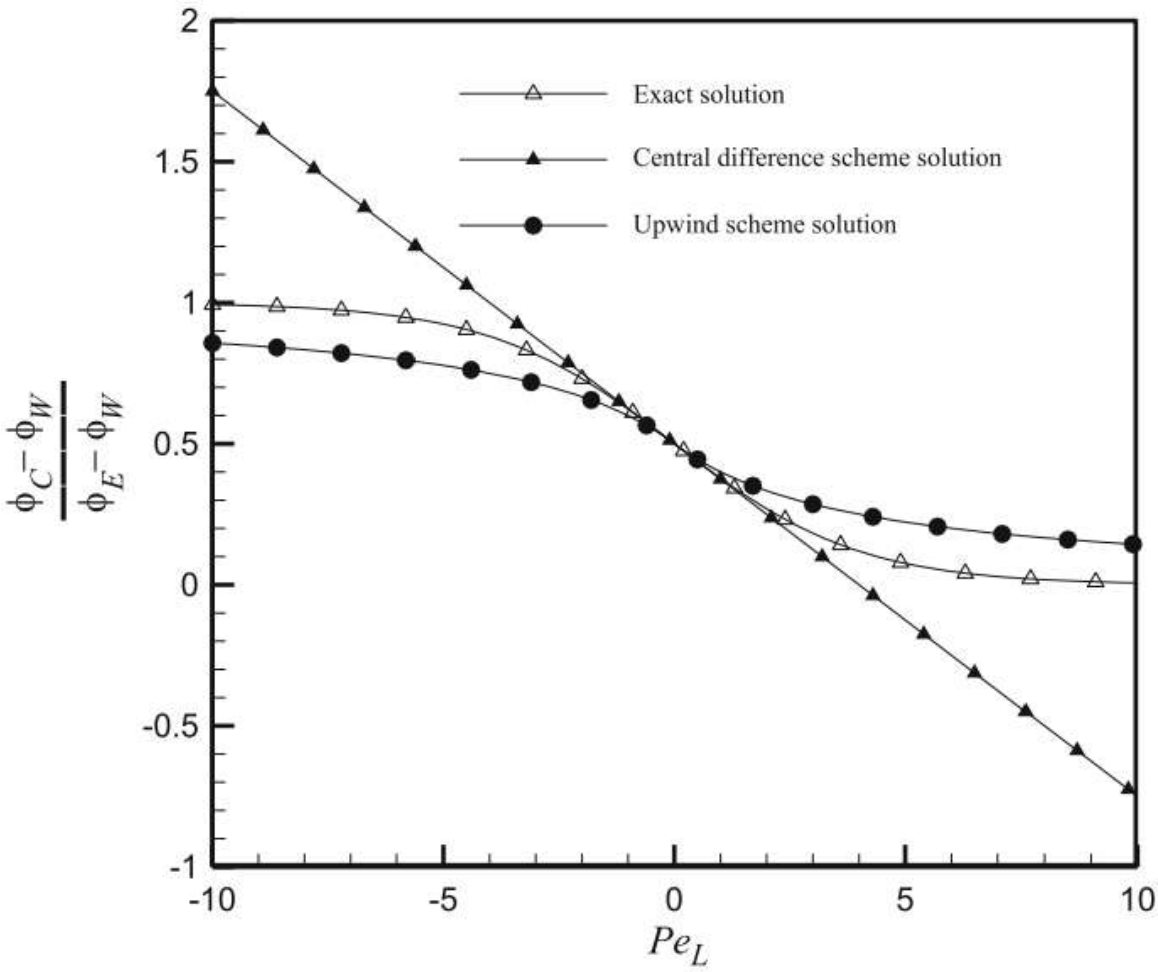

FIGURE 3.3: Comparison between analytical and numerical solution for diffusion-convection problem [6].

Upwind scheme

To overcome the problems of the linear scheme, the upwind scheme considers that the value at the face is to the value at the centroid of the control volume that the mass flow originates.

While this scheme is bounded even at high Pe_L, Fig. 3.3, it is only first order accurate.

The opposite of the upwind scheme, named the downwind scheme, shows that it becomes unbounded but it can be used with other schemes for sharp interfaces.

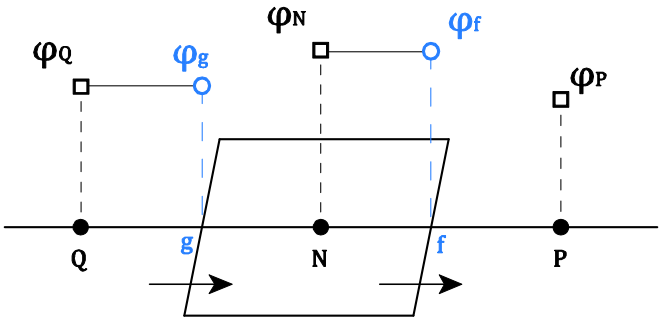

FIGURE 3.4: Upwind scheme.

Second order upwind scheme

This scheme follows the same idea for the derivation of the *upwind scheme,* but the face value is derived by extrapolating linearly two upwind nodes. This scheme is second order accurate.

$$\varphi_f = \frac{3}{2}\varphi_N - \frac{1}{2}\varphi_Q \qquad (22)$$

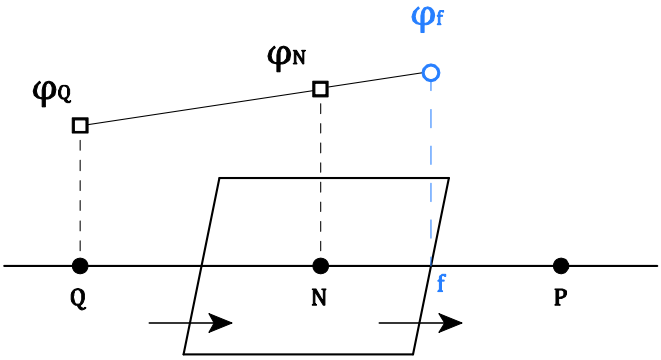

FIGURE 3.5: Second order upwind scheme.

Diffusion term interpolation

As mentioned above, diffusion terms include gradients. Diffusion interpolation is affected by the orthogonality of the mesh. This issue derives from the cell-centred arrangement preferred by the Finite Volume Method. If the normal vector of the interface between two cells is collinear to the vector connecting the respective centroids then the cells are connected orthogonally. In that case, the face value of the diffusive term is calculated from the first order derivative:

$$\vec{S} \cdot (\nabla\varphi)_f = |\vec{S}| \frac{\varphi_N - \varphi_Q}{|\vec{d}|} \quad (23)$$

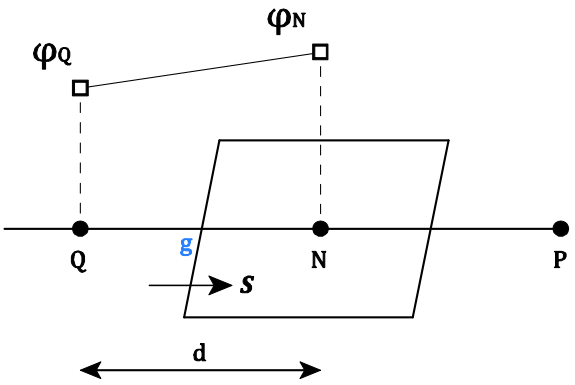

FIGURE 3.6: Diffusion gradient interpolation.

However, most meshes are not entirely orthogonal owing to the complex fluid flows. As a consequence, the interface normal flux vector $\boldsymbol{S_f}$, can be derived from the orthogonal contribution component $\boldsymbol{E_f}$, that is calculated from the first order derivative and a correction component $\mathbf{T_f}$, named cross-diffusion or non-orthogonal diffusion, as shown in Fig. 3.7:

$$\overrightarrow{S_f} = \overrightarrow{E_f} + \overrightarrow{T_f} \quad (24)$$

The non-orthogonal correction factor can be modeled by one of the following methods:

$$(\nabla\varphi)_f \cdot \overrightarrow{T_f} = \begin{cases} (\nabla\varphi)_f \cdot (\vec{n} - \cos\theta\, \vec{e}) S_f \\ (\nabla\varphi)_f \cdot (\vec{n} - \vec{e}) S_f \\ (\nabla\varphi)_f \cdot \left(\vec{n} - \dfrac{1}{\cos\theta}\vec{e}\right) S_f \end{cases} \quad (25)$$

The first, the minimum correction method, makes $\boldsymbol{E_f}$ and $\boldsymbol{T_f}$ orthogonal to minimise the correction factor. the second is called the normal correction method while the last is the over-relaxed method which is commonly used due to its' stability on highly non-orthogonal meshes.

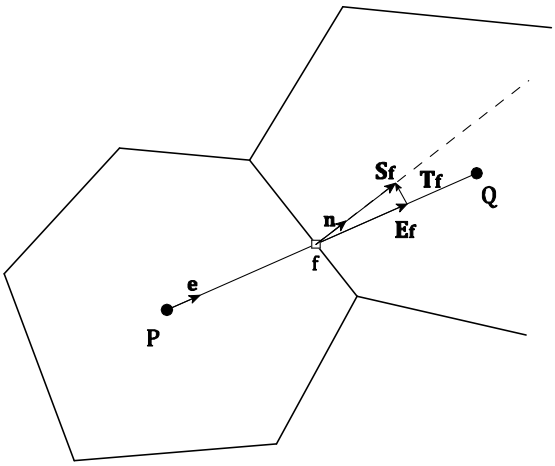

FIGURE 3.7: Non-orthogonality correction.

In the case that mesh is skewed, the centroid connecting vector does not intersect the interface's centroid, Fig. 3.8, meaning that interpolation techniques fail to approach the correct face value. The value at the face centre *f*, is calculated using the value at the intersection *f'* and a correction derived from the derivative at *f'*.

$$\varphi_f = \varphi_{f'} + (\nabla\varphi)_{f'} \cdot \boldsymbol{d}_{f'f} \qquad (26)$$

Where, $\boldsymbol{d}_{f'f}$ the vector from *f'* to *f*.

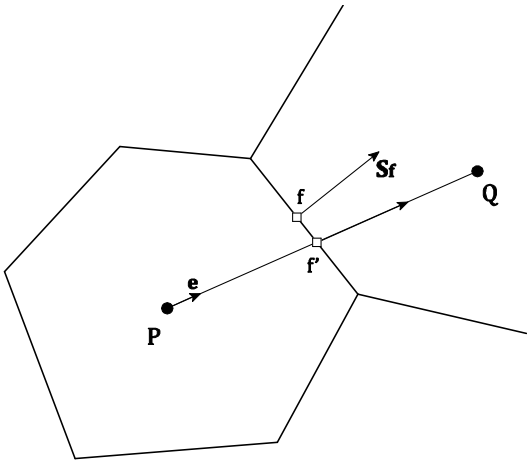

FIGURE 3.8: Non-conjunctional elements.

Source term discretisation

The most common source term example of source terms is a chemical reaction. Nevertheless, source terms appear in various other cases. Usually, source terms depend on the variable of interest. The term is discretised using a Taylor series which is manipulated to include an explicit

part that is calculated from the results of the previous iteration and an implicit part that includes the variable of interest:

$$S(\varphi_C) = \left(\frac{\partial S}{\partial \varphi_C}\right)^* \cdot \varphi_C + S(\varphi_C^*) - \left(\frac{\partial S}{\partial \varphi_C}\right)^* \cdot \varphi_C^* \quad (27)$$

The first term represents the implicit part, while the other two the explicit part. Terms denoted with asterisk superscript (*), derive from the previous iteration.

Computation of incompressible fluid flows

The previous discretisation schemes dealt with the linearisation of a general transport equation which require the knowledge of the velocity field. However, owing to the coupled nature of the pressure and velocity fields, the solution of the Navier-Stokes equations is not straightforward. For simplicity, only the continuity and momentum equation are considered in the following analysis. These form a set of four equations which are used to find the four unknown values (U_x, U_y, U_z, p). Nevertheless, after close observation it can be observed that there is no equation for the pressure calculation. In fact the continuity equation consists in a restriction on the x, y and z velocity componets' values derived from the momentum equations, meaning that the solution of the momentum equations must satisfy the continuity equation restriction. Patankar and Spalding proposed the SIMPLE (Semi Implicit Method for Pressure Linked Equations) algorithm. The main features of the algorithm are the derivation of a pressure equation from the continuity and momentum equations and a velocity field corrector to satisfy the continuity equation. The momentum equation can be written in matrix form as:

$$\boldsymbol{M}U = -\nabla p \quad (28)$$

In which the coefficients of matrix **M** are known. Then, matrix **M** is split into diagonal and off-diagonal components:

$$\boldsymbol{A}U - \boldsymbol{H} = -\nabla p \quad (29)$$

Where, $\boldsymbol{H} = \boldsymbol{M}U - \boldsymbol{A}U$, and **A** the diagonal matrix. Diagonal matrices can be inverted easily, yielding an equation for velocity:

$$U = \boldsymbol{A^{-1}H} - \boldsymbol{A^{-1}}\nabla p \quad (30)$$

Which is subsequently substituted into the continuity equation, resulting in a pressure equation:

$$\nabla \cdot U = 0 \Longrightarrow \nabla \cdot [\boldsymbol{A^{-1}H} - \boldsymbol{A^{-1}}\nabla p] = 0 \Longrightarrow \nabla \cdot (\boldsymbol{A^{-1}}\nabla p) = \nabla \cdot (\boldsymbol{A^{-1}H}) \quad (31)$$

The solution procedure of the SIMPLE algorithm consists in the following steps:

1. The pressure field that resulted in the previous iteration is used in the momentum equation (28) to derive a velocity field which does not conserve mass meaning that the continuity equation is not satisfied,
2. The resultant velocity field is used to form the pressure correction equation (31),
3. The velocity field is corrected using the equation (30).

This procedure is repeated until both continuity and momentum equations are satisfied simultaneously. In this analysis only momentum and continuity equations were considered. Additional energy, turbulence or other transport equations can be solved inside the iterative process.

The pressure-velocity coupling, mentioned above, is enforced by using a staggered grid for the variable values storage to avoid the necessity of interpolations to calculate the pressure gradient and the velocity. Pressure values are stored at the cell centroid, while velocity values at the faces.

Temporal discretisation

The previous paragraphs were involved with the diffusion, convection and source terms. The schemes are common for both steady-state and transient simulations. Transient equation differs from steady-state due to the presence of the temporal derivative which also needs to be discretised. The finite volume approach is similar to the methodology used to discretise the convection term. Consider the following transient expression of a variable φ:

$$\frac{\partial(\rho\varphi)}{\partial t} + \mathcal{L}(\varphi) = 0 \qquad (32)$$

In which the function $\mathcal{L}$ represents all the spatial terms. Integration and spatial discretisation leads to:

$$\frac{\partial(\rho_C\varphi_C)}{\partial t}V_C + \mathcal{L}(\varphi_C^t) = 0 \qquad (33)$$

The finite volume approach eventually leads to:

$$\frac{V_C(\rho_C\varphi_C)^{t+\frac{\Delta t}{2}} - V_C(\rho_C\varphi_C)^{t-\Delta t/2}}{\Delta t} + \mathcal{L}(\varphi_C^t) = 0 \qquad (34)$$

Similarly to the convection interpolation, flux values at times (t), (t+Δt), and so on, are considered as the values at the centroid while those at times (t+Δt/2), (t+3Δt/2), and so on, are the face values.

First order implicit Euler scheme

As in the upwind scheme for the convection term, the flux value at the time-face equals to the value at the upwind centroid.

$$(\rho_C \varphi_C)^{t+\frac{\Delta t}{2}} = (\rho_C \varphi_C)^t \quad (35a)$$

First order explicit Euler scheme

As in the downwind scheme for the convection term, the flux value at the time-face equals to the value at the downwind centroid.

$$(\rho_C \varphi_C)^{t+\frac{\Delta t}{2}} = (\rho_C \varphi_C)^{t+\Delta t} \quad (35b)$$

Crank-Nicholson

As in the central difference scheme for the convection term, the flux value at the time-face derives from interpolation between the two time-adjacent centroids:

$$(\rho_C \varphi_C)^{t+\frac{\Delta t}{2}} = \frac{1}{2}(\rho_C \varphi_C)^{t+\Delta t} + \frac{1}{2}(\rho_C \varphi_C)^t \quad (35c)$$

Initial Conditions

The first timestep represents a temporal boundary as it does not have an upwind neighbour. Consequently, the lower face value is used instead of the centroid's leading to a substantial error since the temporal difference between the two faces is Δt. The issue is dealt with by introducing a first iteration that is $\Delta t/2$ long.

Under-Relaxation

Eventually, the above discretised equations form a system that has to be solved. An initial solution is given to start the iterative procedure which is usually a random estimation of the user. Moreover, many problems involve non-linear physics. As a result, the linearised equations may fail to approximate the solution if the iterative steps are too fast. To overcome this issue, the most common method to increase accuracy is the introduction of the explicit under-relaxation. The solution, after every iteration, is corrected using a relaxation factor λ:

$$\varphi = \varphi' + \lambda(\varphi'' - \varphi') \quad (36)$$

Where, φ' is the previous iteration solution, φ'' is the solution of the current iteration and φ the corrected solution.

Under-relaxation happens when λ<1. The new solution is corrected by decreasing the difference between two consecutive iterations. Obviously, the speed of the solution is reduced. If λ=1, then, there is no relaxation and the new solution is kept unchanged. Values higher than 1 are also accepted and used in cases that a faster convergence is necessary. However, it can lead to instabilities of the solution.

Stability of transient simulations

The execution of a transient simulation requires the definition of the time-step Δt. The selection of the time-step can be determined by the Courant number, which is calculated by:

$$C = \frac{U \cdot \Delta t}{\Delta x} \quad (37)$$

Where,

U is the velocity magnitude;

Δx is the element's length.

The Courant number expresses the speed that information travels in one time-step, in terms of elements. The stability condition states that the Courant number C must be smaller than a maximum value which depends on the method used. In explicit methods the maximum value is 1, while implicit methods can be solved with a larger Courant number value.

Boundary conditions

Various boundary conditions are available but the most common are the value and flux specified boundary conditions also known as Dirichlet and Neumann, respectively. The former imposes a specific value of the variable at the boundary from which the flux can be calculated. On the other hand, the Neumann boundary condition defines directly the flux at the boundary.

Wall boundary conditions

Moving or stationary walls are represented in general by no-slip boundary conditions. This implies that the velocity of the fluid at the wall equals the wall's velocity. The flux normal to boundary is zero and the shear stresses are tangential to the wall.

Inlet boundary conditions

An inlet boundary can be represented by specifying the velocity field or by specifying the static/total pressure and the velocity direction.

Outlet boundary conditions

For outlet boundaries, it is necessary to specify static pressure, mass flow rate or set the boundary condition as a fully developed flow.

Symmetry boundary conditions

The normal gradient of the scalar quantity is set to zero. The velocity vector, on the other hand, keeps the same magnitude and direction for the parallel to the symmetry boundary component while having a zero normal to the boundary component. In other words, the shear stress is zero while the normal stress on the boundary is non-zero.

4. Thrust bearings

Principles of operation

As mentioned above, thrust bearings consist of 2 solid bodies separated by a film of lubricant. To explain the mechanics, a slider bearing is considered, as that represented in Fig. 4.1. Due to the no-slip condition, layers of the lubricating film near the solid walls have the same velocity as the boundaries. Consequently, the runner drags lubricant inside the wedge formed by the runner and the pad, increasing the pressure. As stated by continuity, the mass inflow must be equal to the outflow. Since the inlet opening is larger, the velocity at the outflow must be higher resulting in a decrease in pressure that reaches the ambient pressure. Therefore, a pressure distribution as that shown in the image below should develop.

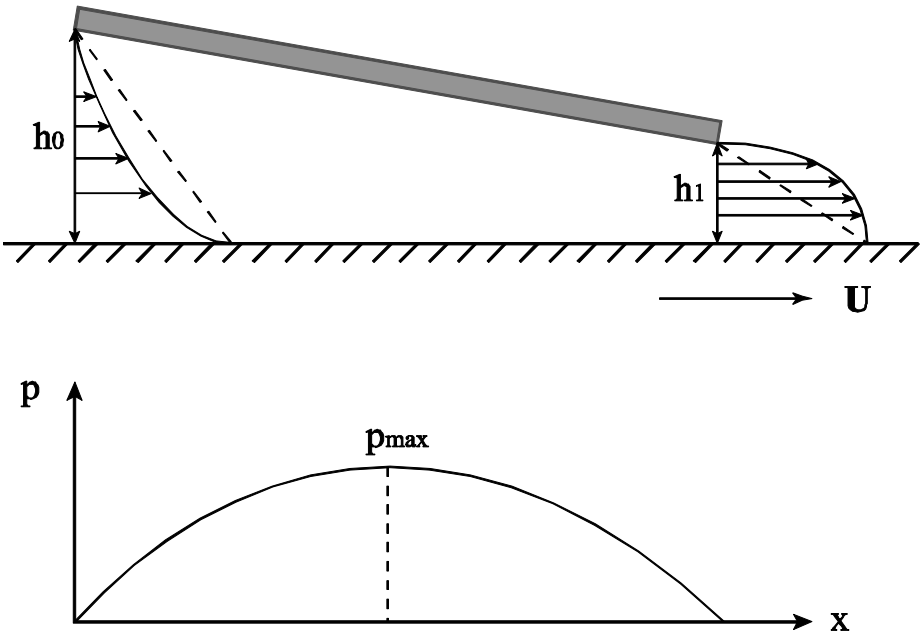

FIGURE 4.1: Pressure generation between non-parallel surfaces.

Reynolds derived the following equation to calculate the pressure distribution considering an incompressible fluid:

$$\frac{\partial}{\partial x}\left(\frac{h^3}{\mu}\frac{\partial p}{\partial x}\right)+\frac{\partial}{\partial y}\left(\frac{h^3}{\mu}\frac{\partial p}{\partial y}\right)=6U\frac{dh}{dx} \qquad (38)$$

To derive the equation, Reynolds made the following assumptions to simplify the physics of the problem:

1. All body forces are neglected which is correct as no external forces act on the fluid apart from magnetohydrodynamic fluids,

2. Fluid pressure does not vary across the film thickness. Apart from elastic fluids, the assumption is valid since the thickness is micrometer small,
3. The oil to rotor and pad interfaces are no-slip boundaries,
4. The fluid is Newtonian, which is not always true, as in cases where a polymeric oil is used as a lubricant,
5. The flow is laminar, which is not true in big turbine applications,
6. Fluid inertia is neglected. For greater accuracy analysis, this term should be considered,
7. Constant fluid density. Not valid for gases, while it is almost true for fluids when thermal expansion is low
8. Constant viscosity throughout the film. This assumption is always incorrect but greatly reduces the complexity.

It can be seen that the pressure distribution is affected from the oil's viscosity μ, the runner's speed U and the geometry of the wedge represented by $\frac{dh}{dx}$. The load can be then calculated from the integral of the pressure distribution:

$$W = \iint_A p dx dy \quad (39)$$

On the other hand, friction is the result of shear stresses, which are defined as $\tau = \mu \frac{\partial u}{\partial y}$ from the viscosity definition of Newtonian fluids. Therefore, the friction force can be calculated from the integral:

$$F = \iint_A \tau dx dy \quad (40)$$

The above analysis considers only the continuity and momentum equations giving results for pressure and velocity. However, due to the shear acting on the fluid, viscous dissipation causes heat generation which increases the lubricant's temperature. As explained previously, the properties of oil lubricants depend on the temperature. Therefore, the energy equation should be included to account for the variation of the lubricants' properties.

Dynamic behaviour

Fluid film thrust bearings are an excellent method to support axial load of rotating machines. While the friction developed is higher compared to ball/roller bearings, fluid film bearings have no wear when operating under constant hydrodynamic lubrication. In addition, they can support large loads as well, such as the thrust that a propeller produces. Finally, the fluid lubricant offers

a significant damping effect that simple ball bearings do not have, leading to lower noise and vibration.

Methodology

In order to predict its' dynamic behaviour, the thrust bearing is represented by a single degree of freedom model. Owing to the fact that the rotor is not supported it may move axially or tilt about a radial axis. In the present work, only axial motions are considered, thus the equation that describes the change of the displacement x of the mass due to a transient load $F(t)$ is the following differential equation:

$$m \cdot \frac{d^2x}{dt^2} + c \cdot \frac{dx}{dt} + k \cdot x = F(t) \quad (41)$$

On the left hand side, the first term represents the inertia forces, the second term expresses the damping forces, while the third term represents the restoring forces known from Hooke's law.

As a result, the stiffness and damping coefficients must be calculated. In addition, due to the fluid nature of oil lubricants, the coefficients k and c are non-linear and compression-only meaning that:

$$k = k(x;\ \omega) \quad (42a)$$

$$c = c(x, \dot{x}; \omega) \quad (42b)$$

In order to calculate the stiffness and damping coefficient, a thermohydrodynamic (THD) CFD analysis was conducted. The analysis is separated into two parts: a steady state, in which a constant minimum film thickness x is imposed to the bearing and the load F_{static} is determined, followed by a transient simulation. F_{static} is the load that the bearing supports under steady operating conditions. In this way, damping and inertia forces are absent and the stiffness coefficient can be calculated for each displacement-load couple, from the Hooke's law equation.

$$k(x) = \frac{F_{static}}{x} \quad (43)$$

The second part eventually leads to the damping coefficient calculation. Unlike the stiffness coefficient, it also depends on the direction of motion and as a result two separate simulations have to be executed. Both force a perturbation of the minimum film thickness by moving the rotor with constant acceleration. The rotor is moved to either approach or move away from the pad, to decrease or increase, respectively, the minimum film thickness. The simulation time t_{total} is split into two parts. The first lasts for 1/3 of the total simulation and no motion is applied. The minimum film thickness stays constant. Subsequently, in the second part the rotor is moved with

constant acceleration, which is described from the following equation, due to the zero initial velocity:

$$x = x|_{t=t_0} \pm \frac{1}{2}\ddot{x} \cdot t^2 \quad (44)$$

The simulation time is set accordingly to achieve a maximum displacement Δx, which in this case is equal to ±0.1 μm. The simulations are repeated for various acceleration values, namely, 1, 5 and 10 m/s^2.

A new force F_{trans} results from each transient simulation and the dynamic part can be calculated after a new steady state simulation at the final minimum film thickness.

$$F_{trans}\left(x \pm \Delta x, \frac{dx}{dt}, \frac{d^2x}{dt^2}; \omega\right) = F_{static}(x \pm \Delta x; \omega) + F_{dynamic}\left(x \pm \Delta x, \frac{dx}{dt}, \frac{d^2x}{dt^2}; \omega\right) \quad (45)$$

At this point, it should be noted that another steady state simulation is required at the position $x \pm \Delta x$. Eventually, the dynamic coefficients for approaching and distancing motions are calculated:

$$c_{approaching}\left(x, \frac{dx}{dt}, \frac{d^2x}{dt^2}; \omega\right) = \frac{F_{dynamic,approaching}}{\dot{x}} = \frac{F_{dynamic,approaching}}{\ddot{x} \cdot t_{total}} \quad (46a)$$

$$c_{distancing}\left(x, \frac{dx}{dt}, \frac{d^2x}{dt^2}; \omega\right) = \frac{F_{dynamic,distancing}}{\dot{x}} = \frac{F_{dynamic,distancing}}{\ddot{x} \cdot t_{total}} \quad (46b)$$

Single degree of freedom setup

The knowledge of the stiffness coefficient $k(x, \omega)$ and the damping coefficient $c(x, \dot{x}, \omega)$ allows the setup of a single degree of freedom model using MATLAB/Simulink software. Given a transient load *F(t)*, the model calculates the response of the bearing by the single degree of freedom equation stated previously which can be written as:

$$\ddot{x}(t) = \frac{1}{m}[F(t) - c \cdot \dot{x}(t) - k \cdot x(t)] \quad (47)$$

The bearing setup is always under a state of compression and the rest position is supposed to be where the minimum film thickness is equal to h_{rest}. Two distance vectors are used by the model. Initially, the rotor is placed at the rest position and no external force is acted upon. Any load displaces the rotor from this position at a distance *x*, depending on the magnitude, compressing

the rotor. Consequently, the minimum film thickness h decreases by x. Thus, as depicted in Fig. 4.2:

$$h(t) = h_{rest} - x(t), \qquad x, h \; in \; \mu m \tag{48}$$

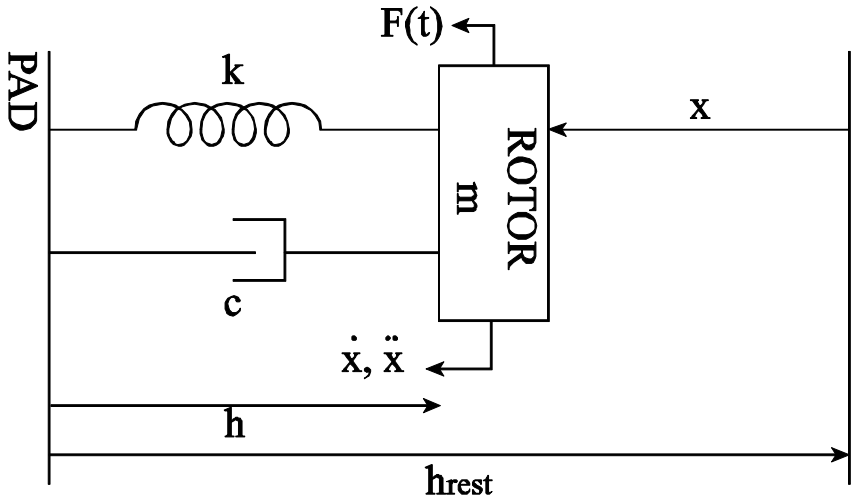

FIGURE 4.2: Single degree of freedom model represantation

Equation (47), above, is used to calculate the acceleration at each time-step. Zero initial conditions are set for the displacement ($x(0) = 0\mu m \Leftrightarrow h(0) = h_{rest}$) and the velocity. Time integration calculates the velocity and the displacement at the specific time-step. Subsequently, as explained by the algorithm in Fig. 4.3, stiffness and damping coefficients are extracted from the maps created and the restoring and damping forces are defined. This procedure highlights the fact that acceleration is not known beforehand. While the stiffness coefficient only requires the minimum film thickness to be defined the damping coefficient is also a function of the velocity and acceleration as stated above. To deal with the issue, all the interpolations for the damping coefficient relationship with acceleration are done considering that acceleration is equal to the RMS value of the load's acceleration $a_{load}(t) = {}^{F(t)}/_{m}$. Both distancing and approaching coefficients are calculated but the correct is selected by determining the motion direction ($\dot{x} > 0 \rightarrow approaching, \dot{x} < 0 \rightarrow distancing$).

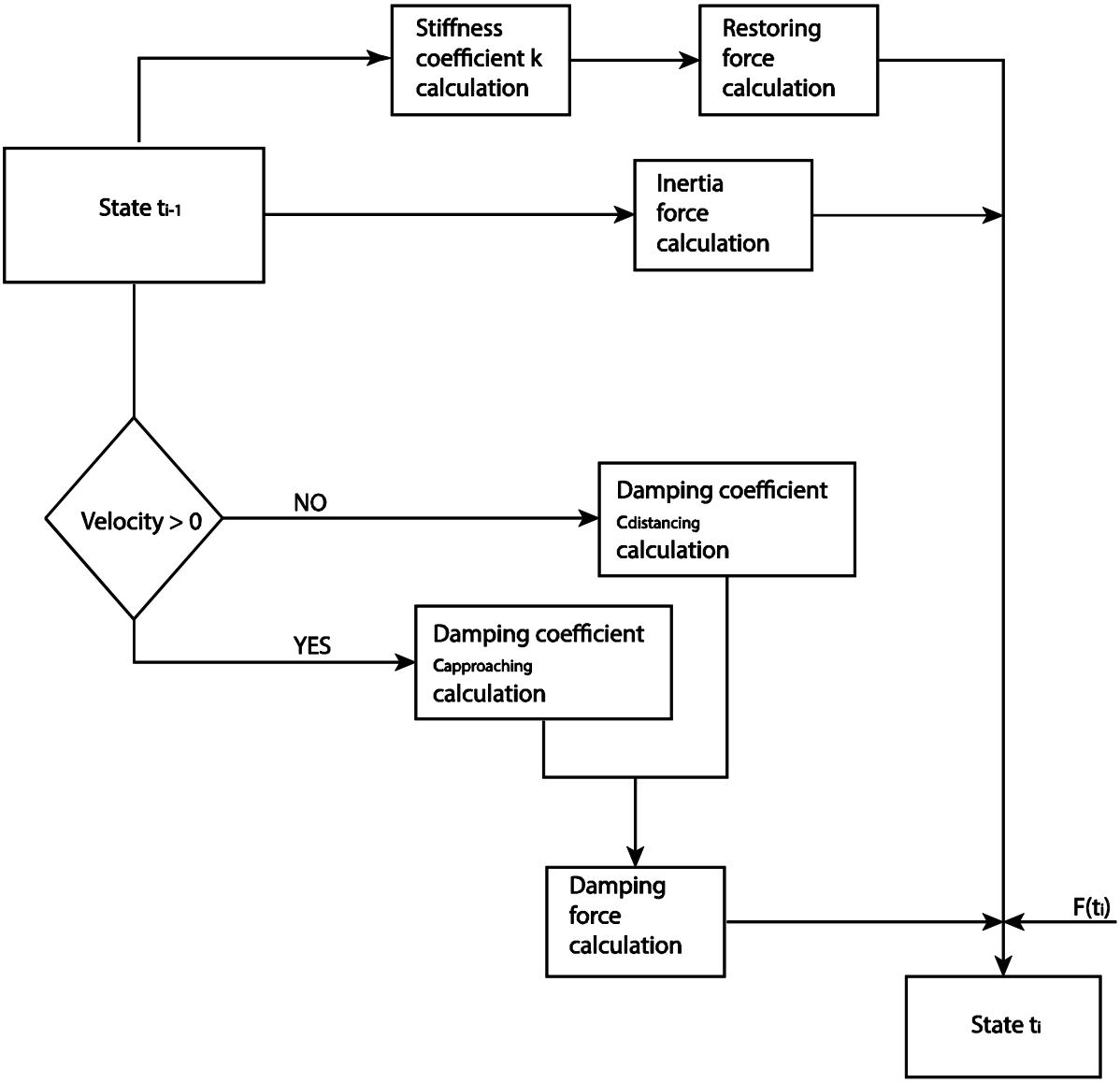

FIGURE 4.3: Single degree of freedom calculations algorithm

5. Case study

Geometry

The geometry considered in the present study consists of an eight-sector pad tapered land thrust bearing. The number of computations necessary is decreased by exploiting the rotational symmetry of a thrust bearing, thus considering only one sector, whose regions are displayed in Fig. 5.1. The fluid region (oil) separates the two solid (rotor, pad). Each of the eight pad sectors consists of an initial groove, a taper region where the film thickness decreases linearly until the land where the pad-rotor distance is constant and equal to the minimum film thickness, as shown in Fig. 5.2 and Fig. 5.3. Rotational periodicity conditions are applied to account for the symmetry of the problem. This requires the inclusion of the following sectors' groove.

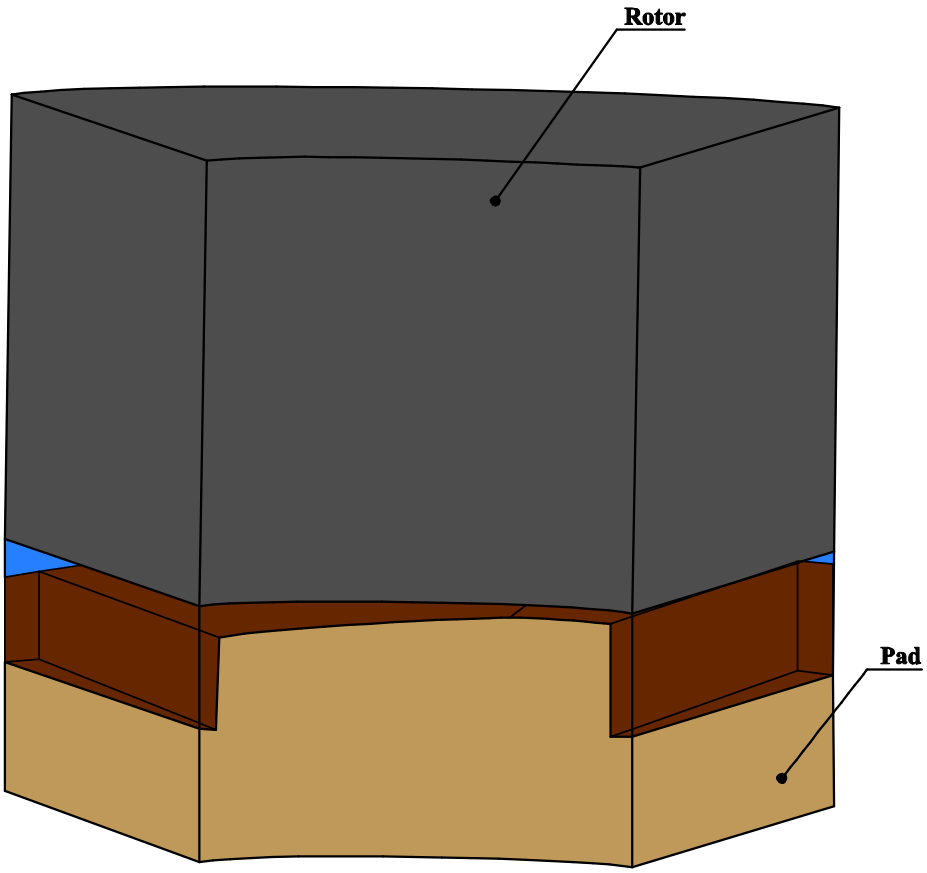

FIGURE 5.1: Domain geometry of rotor and pad separated by fluid film.

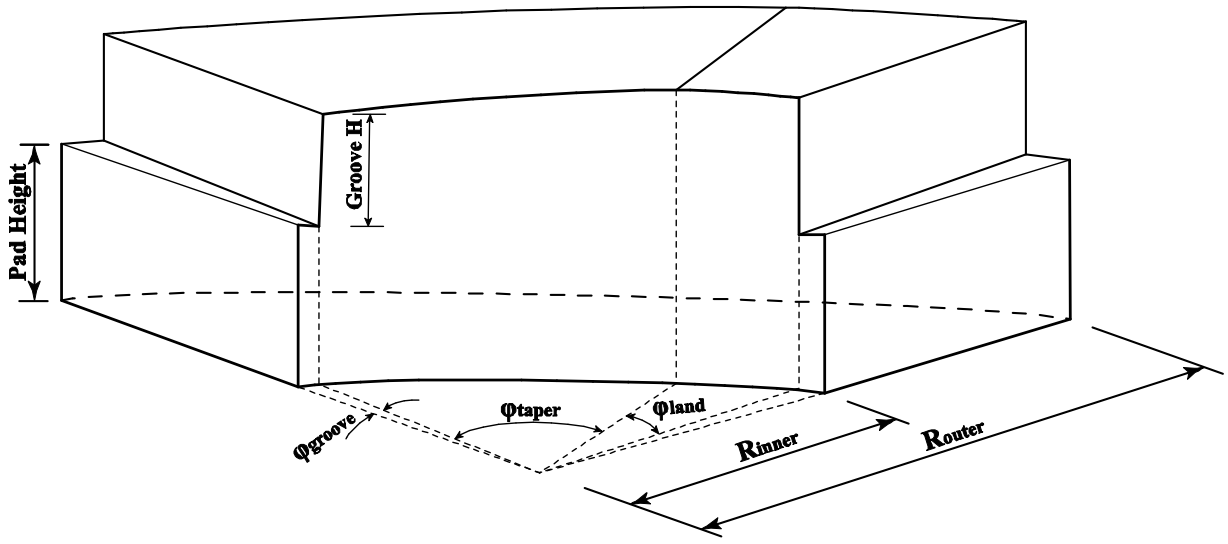

FIGURE 5.2: Geometric characteristics of tapered land bearing's pad.

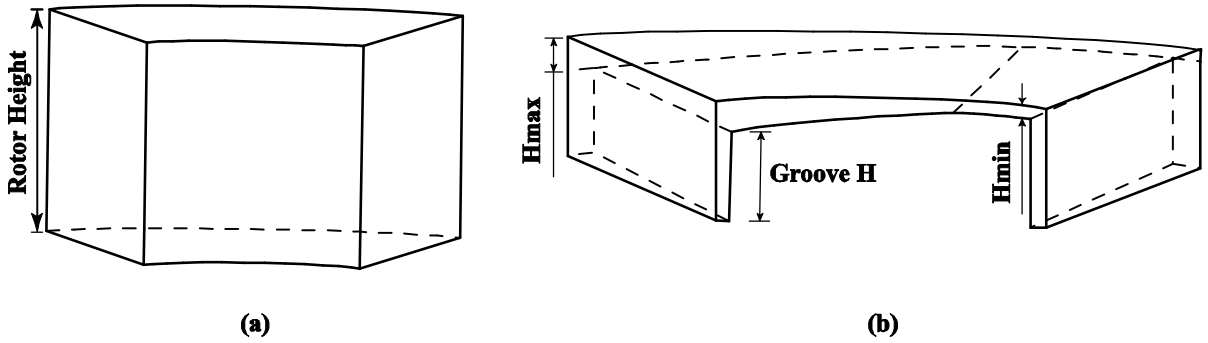

FIGURE 5.3: Geometric characteristics of: (a) rotor, (b) oil.

A parametric analysis has been conducted to define the optimum couple of taper extent and inclination. The analysis has been performed on the minimum film thickness of $H_{min} = 20\ \mu m$, which has been considered to be the operating condition. It examined values of inclination ΔH between 40 and 95 microns, and for each one the taper's extent varied between 55% and 75% of the sector's total angle of extent. For every value of ΔH examined, the design with the best Load to Friction Torque value is selected, as it appears in Fig. 5.2. The results indicate that while the maximum pressure increases as ΔH increases after the optimum point, the load – the pressure integral over the rotor surface- decreases. Moreover, friction torque keeps increasing, eventually leading to the decrease of the load to friction torque ratio.

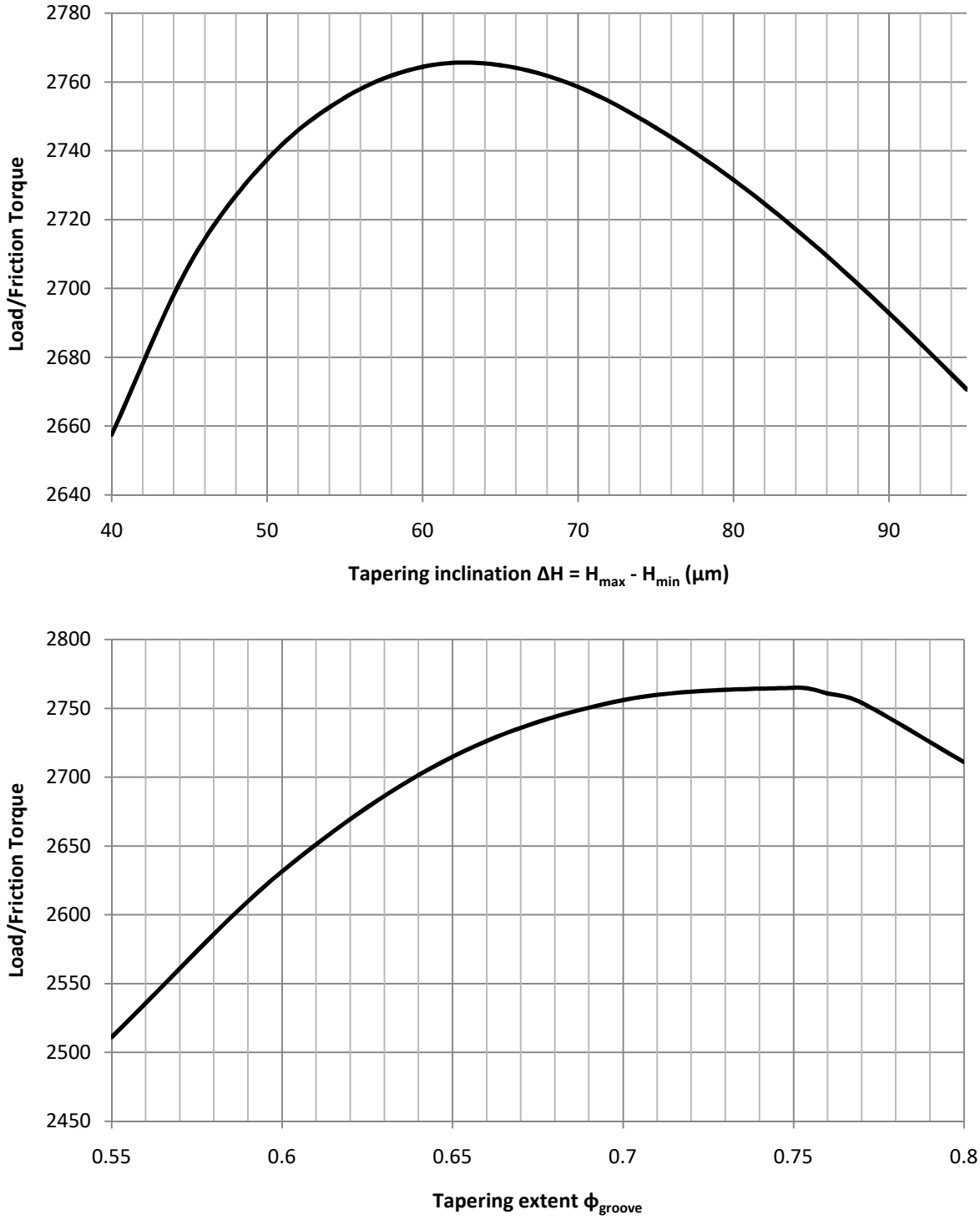

FIGURE 5.4: Results of parametric analysis: (a) Maximum load to friction torque ratio value for every taper inclination value, (b) Load to friction torque ratio for optimum taper inclination case.

Thus, the geometric characteristics finally selected are listed in Table 5.1.

TABLE 5.1: Geometry characteristics.

Description	Symbol	Unit	Value
Number of pads	N_{pad}		8
Diameter (Inner/Outer)	D_{inner} / D_{outer}	mm	50 / 90
Taper inclination	ΔH	μm	65
Groove extent angle	φ_{groove}	° (deg)	2.45
Taper extent angle	φ_{taper}	° (deg)	33.75
Height (Groove/Rotor/Pad)	H_{groove} / H_{rotor} / H_{pad}	mm	4 / 10 / 6

Mesh

A structured mesh totaling approximately 720000 hexahedral elements has been generated, consisting of 121 equal length elements across the circumferential direction, 65 across the radial direction and 92 elements across the height, 10 out of which across the film thickness. Details of the mesh are represented in Fig. 5.2.

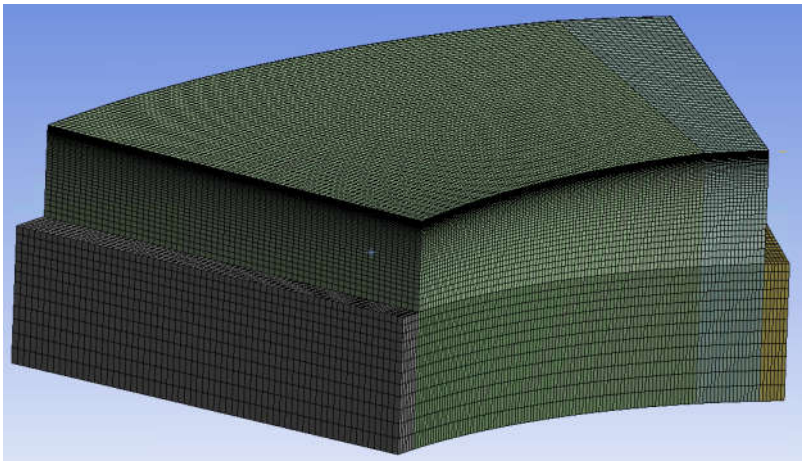

(a)

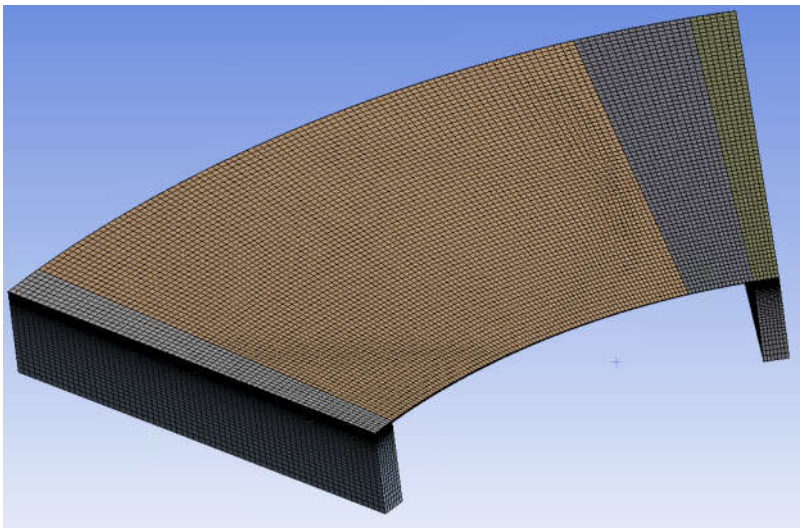

(b)

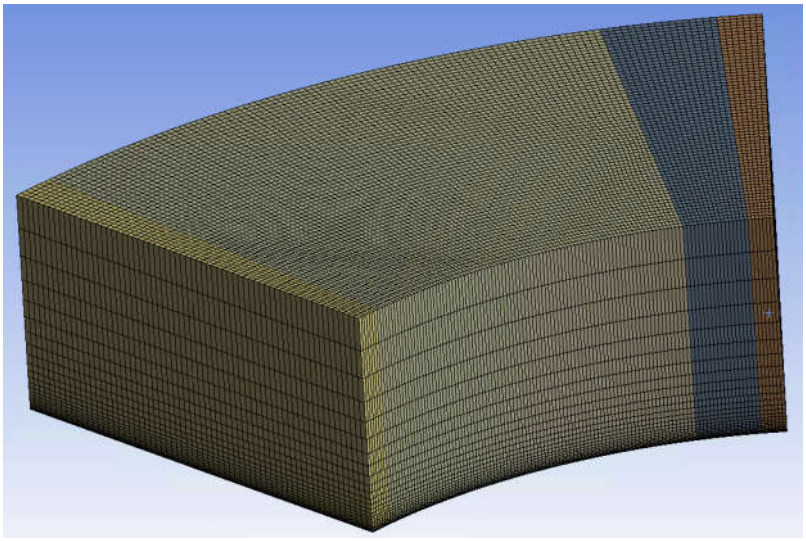

(c)

FIGURE 5.2: Mesh details: (a) Pad, (b) Fluid, (c) Rotor.

Boundary conditions

The boundary conditions used are listed in Table 5.2 for the fluid domain and Table 5.3 for the solid domains and the locations are depicted in Fig. 5.3. Regarding the fluid domain, the internal boundary (named inlet) is considered a pressure inlet. The oil is fed at a constant pressure, however, depending on the pressure distribution in the fluid domain, oil may be pushed out in locations where the pressure is higher than the feeding value. On the other side, the fluid is allowed only to exit through the outlet. In reality, air may enter through this boundary in locations that the pressure inside is lower than the ambient. The outer side of the grooves is covered from the pad's body, thus a wall is placed which does not allow oil outflow. Since only

one pad is considered, the sides are modeled with a rotational periodicity interface to account for the adjacent pads. Finally, the two walls that are on the top and bottom side are the rotor and pad interfaces, respectively. In both cases, thermal effects have been taken into account by considering that the heat flux on either side of the interface is the same. In addition, while the pad is fixed in space, the rotor rotates, dragging the fluid's upper layer due to the no-slip condition. Consequently, the fluid has the same velocity field as the rotor.

TABLE 5.2: Fluid domain boundary conditions.

Fluid domains	Oil	
Inlet	Type:	Opening
	Pressure:	1 bar
	Temperature:	40°C
Outlet	Type:	Outlet
	Pressure:	0 bar
Wall outlet	Type:	No-slip wall boundary
Sides	Rotational periodicity	
Pad interface	Heat flux and temperature continuity	
Rotor interface	Angular velocity:	6000 RPM
	Heat flux and temperature continuity	

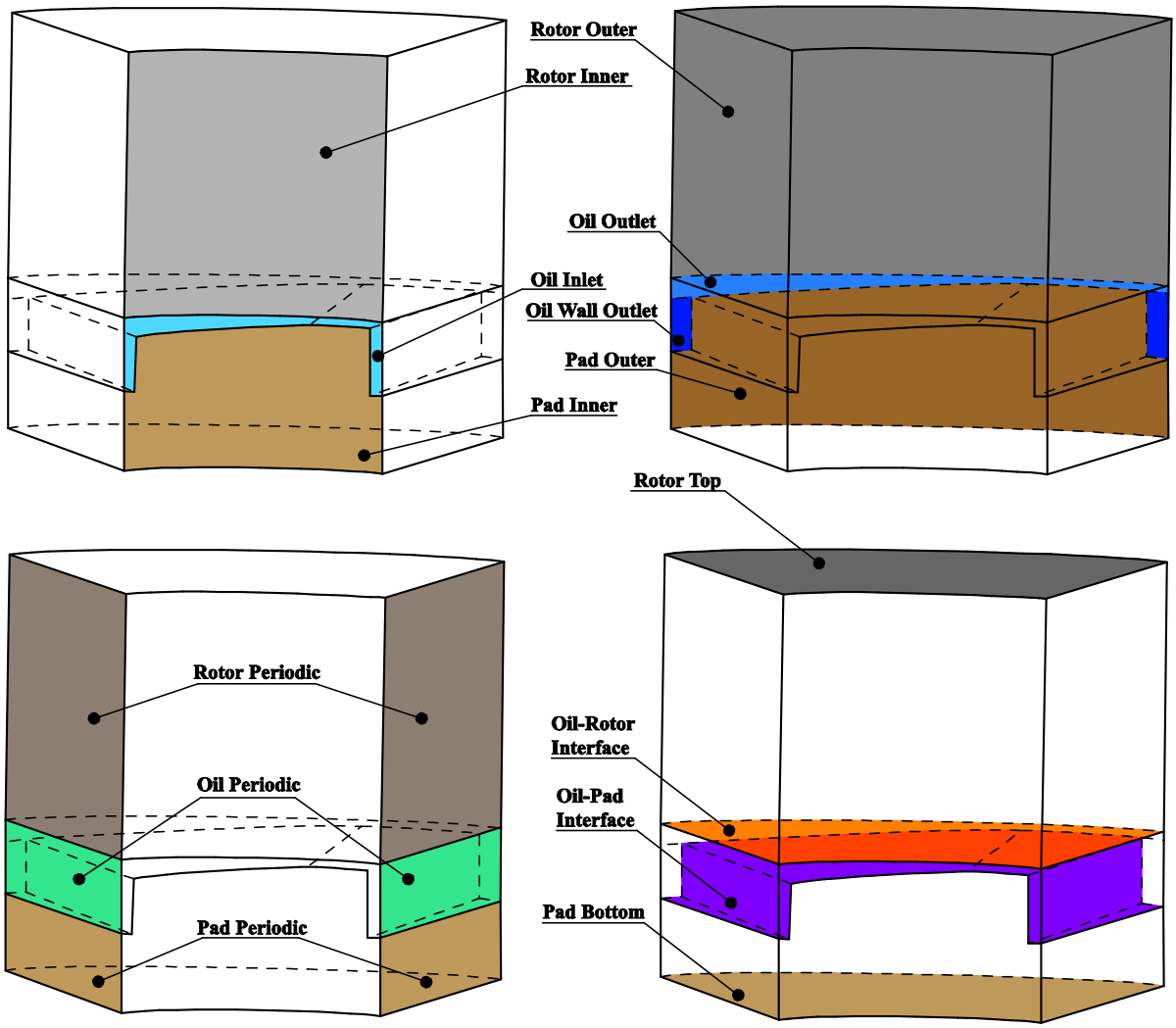

FIGURE 5.3: External boundaries and interfaces.

The thermal boundaries on the solid domains have been set by defining the ambient temperature and a heat transfer coefficient. The pad's inner and bottom sides are in contact with hot oil. Due to the higher velocities on the external side of the inner boundary, the coefficient is greater than that at the bottom side. The pad's outer side is in contact with ambient air, hence the lower ambient temperature. The rotor, usually, is a solid shaft and as a result in the inner side an adiabatic boundary is set, which means that there is a zero temperature gradient normal to the boundary. The remaining boundaries are in contact with ambient air.

TABLE 5.3: Solid domains boundary conditions.

Solid domains	Rotor		Pad	
Inner	Adiabatic boundary		Heat transfer coefficient: Ambient temperature:	750 W/mK 40°C
Outer	Heat transfer coefficient: Ambient temperature:	25 W/mK 25°C	Heat transfer coefficient: Ambient temperature:	25 W/mK 25°C
Top / Bottom	Heat transfer coefficient: Ambient temperature:	25 W/mK 25°C	Heat transfer coefficient: Ambient temperature:	1000 W/mK 40°C
Sides	Rotational periodicity		Rotational periodicity	
Oil interface	Heat flux and temperature continuity		Heat flux and temperature continuity	

Setup

The effect of the moving rotor on the fluid's velocity field was established by setting the same velocity field at the interface. However, the temperature condition is different. Due to viscous dissipation, the oil is heated in high pressure gradient regions. Therefore, the temperature differs both along the circumferential and the radial direction. As the rotor is spinning, a finite area at a specific radial direction encounters different temperature values and eventually reaches a steady state value. However, the solid motion feature on the rotor is extremely time consuming since it requires approximately ten times more steps to reach convergence. In addition, its' effect on the fluid temperature is minor, therefore, it has been neglected.

Additionally, in regions where the pressure drops below the vapour pressure, cavitation occurs. To account for this phenomenon, a Rayleigh-Plesset homogeneous multiphase model has been utilised, in which the vapour is represented by a dispersed fluid.

As for the oil's properties, the difference of the density, specific heat capacity and thermal conductivity values is negligible in the expected temperature range and can be ignored. Thus, they have been considered to be constant. On the other hand, the viscosity has been calculated through the ASTM equation, mentioned above. The details for both the lubricant oil and the vapour phase that has been considered when cavitation occurs are listed in Tables 5.4 and 5.5, respectively.

TABLE 5.4: Oil material details.

Description	Symbol	Unit	Value
Thermodynamic state		Liquid	
Molar mass	M	kg/kmol	383.92
Density	ρ	kg/m^3	870
Specific heat capacity	C_p	J/kgK	2100
Thermal conductivity	k	W/mK	0.13
Kinematic viscosity, 40°C	$\nu_{40°C}$	cSt	47.26
Kinematic viscosity, 100°C	$\nu_{100°C}$	cSt	7.17

TABLE 5.5: Vapour material details.

Description	Symbol	Unit	Value
Thermodynamic state		Gas	
Molar mass	M	kg/kmol	383.92
Density	ρ	kg/m^3	1.185
Specific heat capacity	C_p	J/kgK	1004.4
Dynamic viscosity	μ	$N{\cdot}s/m^2$	2.10E-05
Thermal conductivity	k	W/mK	0.0261

Both rotor and pad have been considered to be made from steel whose details are listed in Table 5.6, below.

TABLE 5.4: Rotor and pad material properties.

Description	Symbol	Unit	Value
Thermodynamic state		Solid	
Molar mass	M	kg/kmol	55.85
Density	ρ	kg/m^3	7854
Specific heat capacity	C_p	J/kgK	434
Thermal conductivity	k	W/mK	60.5

Regarding the dynamic analysis, the moving mass has been considered to be equal to $m = 4\ kg$, while the rest position has been set at a distance of $h_{rest} = 50\ \mu m$. As for the load, the bearing has been initially set at the nominal minimum film thickness distance of 20μm and then the following sum of sinusoidal functions has been applied:

$$F(t) = A_1 \cdot sin\left(\frac{\omega t}{2} + \varphi_1\right) + A_2 \cdot sin(\omega t + \varphi_2) + A_3 \cdot sin(2\omega t + \varphi_3) + A_4 \cdot sin(4\omega t + \varphi_4) + A_5 \cdot sin(8\omega t + \varphi_5) + A_6 \cdot sin(16\omega t + \varphi_6)$$

Where, $\omega = 600\ rad/s$ and the amplitudes and phases those listed in Table 5.5.

TABLE 5.5: Transient load amplitudes and phases

Amplitude	Value	Phase	Value
A_1	30	φ_1	5.353297
A_2	40	φ_2	3.878171
A_3	20	φ_3	0.085219
A_4	15	φ_4	2.010225
A_5	15	φ_5	1.152626
A_6	15	φ_6	3.710464

CFD Results

The steady-state simulation indicates –as expected- that as the minimum film thickness decreases both pressure and temperature increase, as depicted in Fig. 5.4. Both infinitely long and infinitely short assumptions for the Reynolds' equation solution indicate that pressure increases as the film thickness parameter decreases. This is due to the fact that the bearing creates a Couette type flow. The fluid mass dragged into the bearing is mainly affected from the film thickness on the taper inlet. Owing to the decrease in the film thickness in the circumferential direction, pressure must increase as it appears in the contour Fig. 5.5. The greater the film thickness differential, the greater the pressure increase.

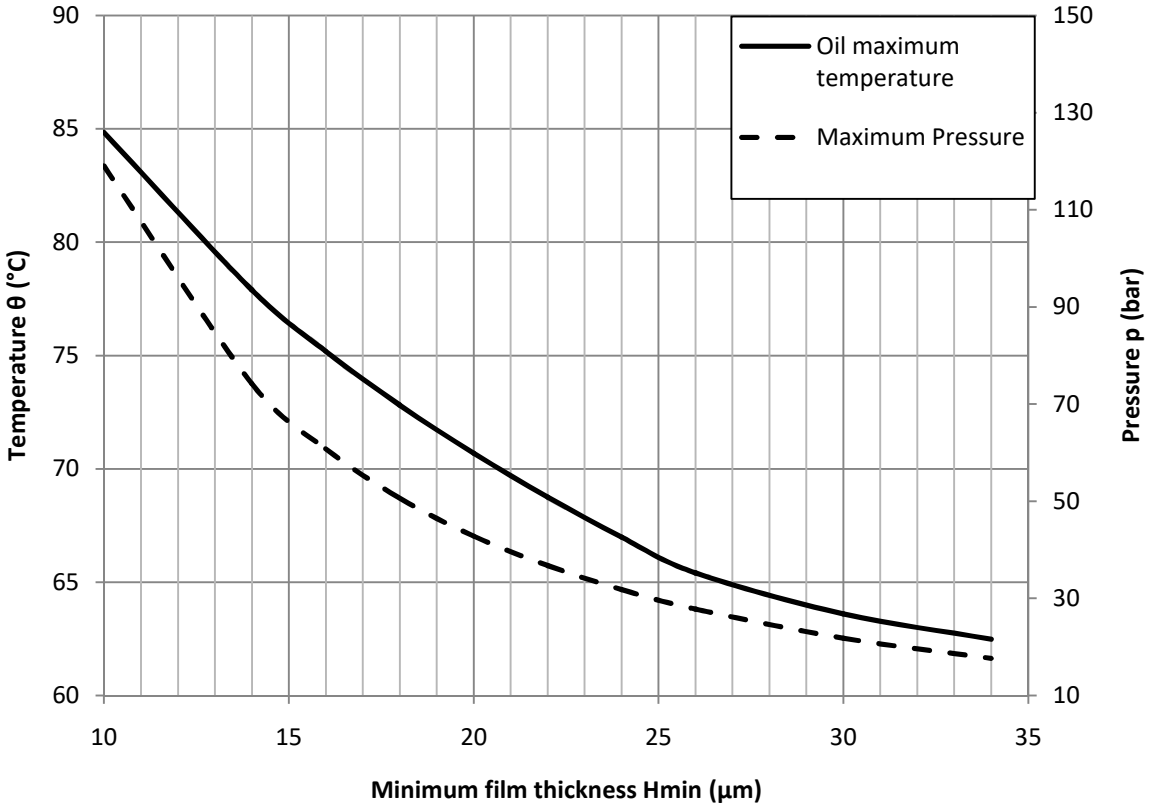

FIGURE 5.4: Maximum pressure and temperature - minimum film thickness diagram.

In Fig. 5.6, the pressure distribution along the circumferential direction at the middle of the bearing's width at the oil-rotor interface is displayed. Inside the groove there is no pressure buildup. In the taper region, pressure increases, reaching its' maximum value at the end of the taper region. Then, it drops quickly to satisfy the periodical boundary conditions.

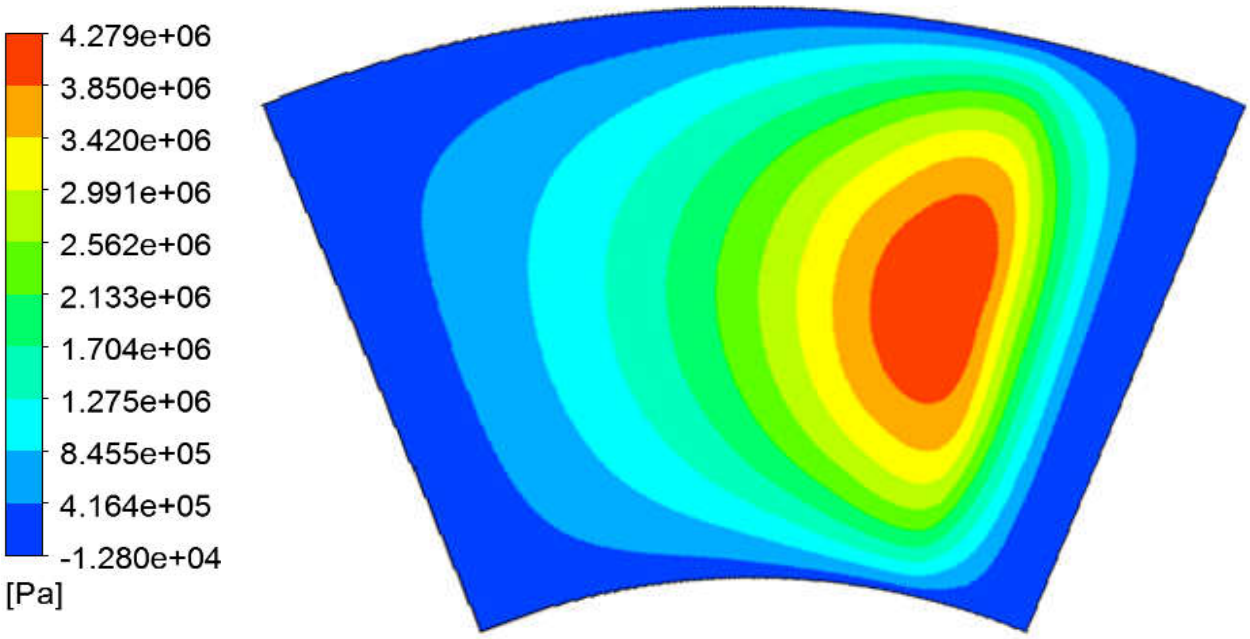

FIGURE 5.5: Pressure contour on oil-rotor interface.

FIGURE 5.6: Circumferential pressure distribution along midline.

Fig. 5.7 displays the pressure distribution across the bearing's width at the circumferential position near the location of maximum pressure. Oil is fed at a pressure of 1 bar. Across the width, pressure increases and reached the maximum value at the middle of the width, then decreases to satisfy the outlet's atmospheric pressure boundary condition.

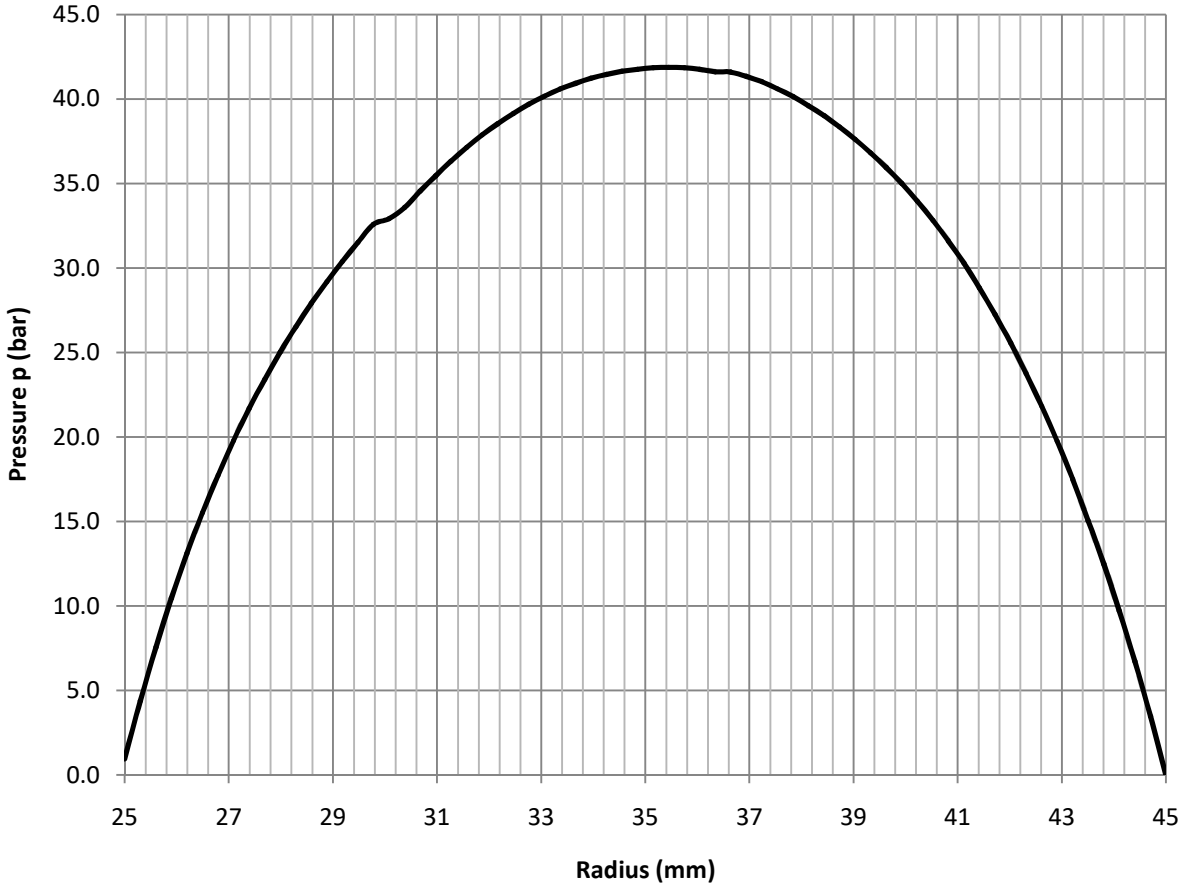

FIGURE 5.7: Radial pressure distribution.

The pressure that has been built up at the end of the taper region prevents the free entrance of the relatively cool oil fed at the inlet. Oil enters through the left side of the pad and is heated as it is dragged circumferentially reaching its' peak value at the right corner of the outlet, as it appears in Fig. 5.8. As a result, the pad's temperature, Fig. 5.9, is greater near the right side where the oil's temperature is higher.

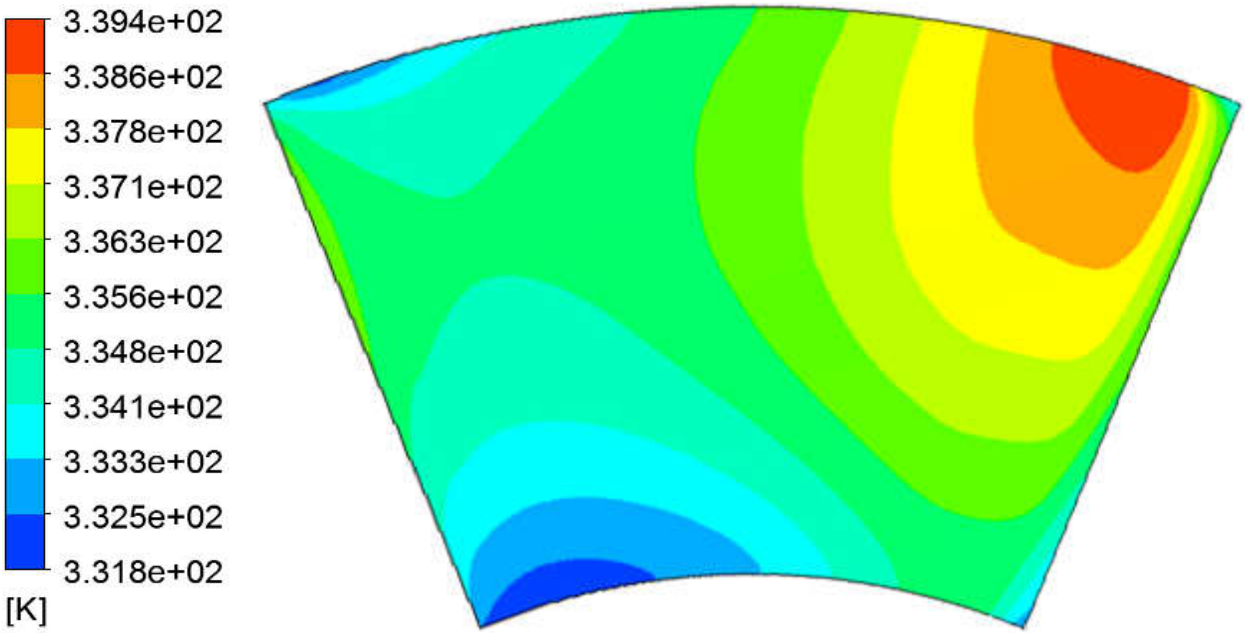

FIGURE 5.8: Temperature contour on oil-rotor interface.

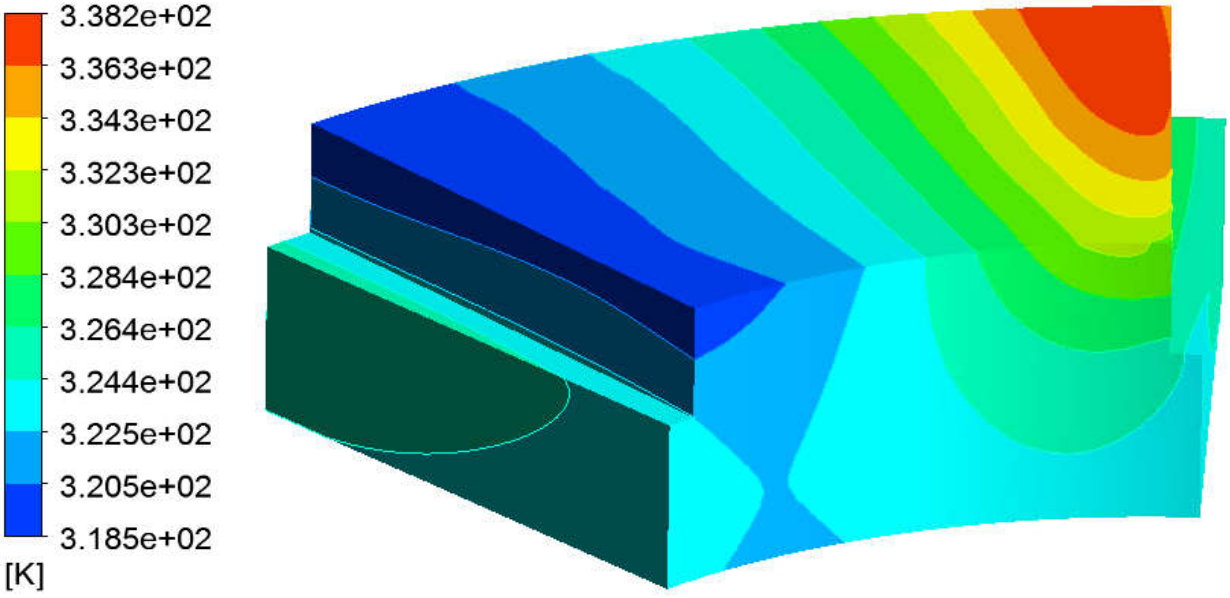

FIGURE 5.9: Pad temperature contour.

Similarly, load and friction torque increase as fluid film thickness decreases as shown in Fig. 5.10. However, friction torque increases less rapidly leading to a greater value of the load to friction torque ratio, which justifies the choice to design more loaded bearings in order to benefit of higher efficiency.

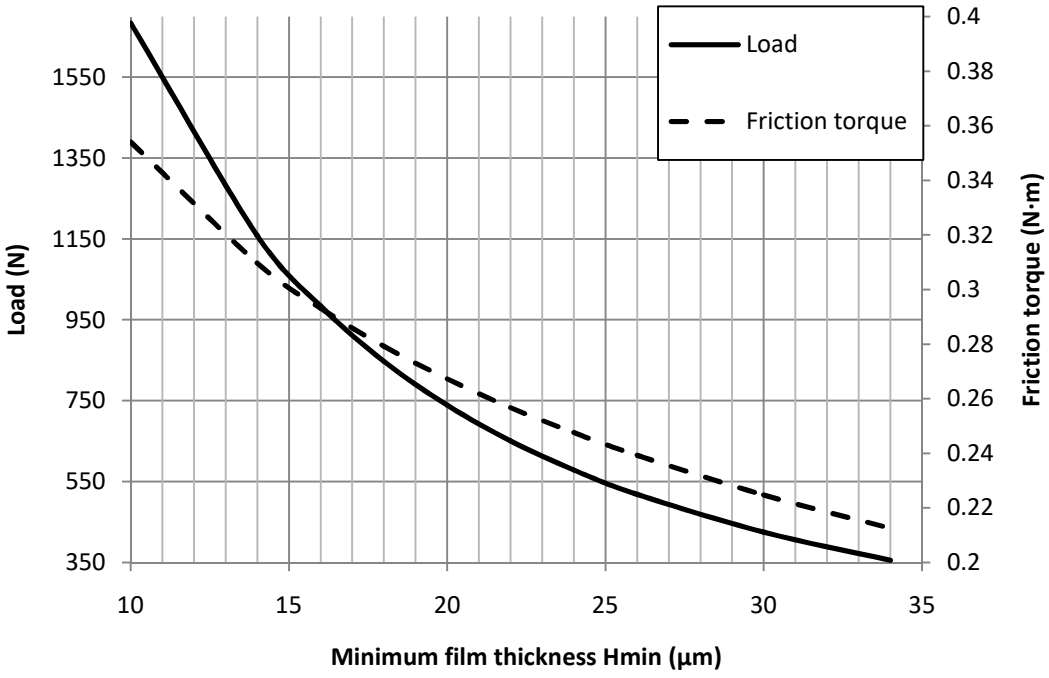

FIGURE 5.10: Load and friction torque - minimum film thickness diagram.

Regarding cavitation, the solution indicates that there is no cavitation occurring.

Regarding the transient simulations, for each minimum film thickness evaluated the steady load and the transient load after a displacement of 0.1 μm to either approach or move away from the pad, are calculated and is listed in Table 5.6. The transient simulations are repeated for three different acceleration values.

TABLE 5.6: Transient load results.

H_{min} (μm)	Steady Load (N)	Transient Load (N)					
		Approaching			Distancing		
		1 m/s^2	5 m/s^2	10 m/s^2	1 m/s^2	5 m/s^2	10 m/s^2
10	1683.95	1,717.29	1,742.51	1,750.00	1,651.75	1,628.28	1,618.76
14	1158.63	1,182.57	1,198.26	1,210.00	1,134.82	1,119.59	1,110.00
16	984.23	1,005.05	1,017.03	1,030.00	964.86	951.77	941.36
18	847.736	864.23	877.22	887.00	831.04	818.62	809.37
20	738.938	754.50	764.68	774.00	723.56	713.50	704.28
22	650.945	663.75	674.29	683.00	637.83	627.90	619.61
24	578.893	590.59	599.81	608.00	567.96	558.18	550.49
26	518.837	529.06	537.92	545.00	508.78	499.94	492.98
30	424.883	432.81	440.29	447.00	417.08	409.62	403.18
34	355.928	362.33	368.92	374.49	349.60	343.06	337.56

The stiffness coefficient has then been calculated and plotted in Fig. 5.11, according to equation (43). It should be noted that as the minimum film thickness decreases the stiffness coefficient decreases non-linearly, since the load also follows a non-linear decrease, as explained above. In addition, the zero value at the minimum film thickness of 50 μm has been set due to the fact that it is considered as a rest position. This is not exactly true since a small load would be calculated if the simulation was conducted. However, this assumption has to be done in order to achieve the correct response in the single degree of freedom and it as been explained below.

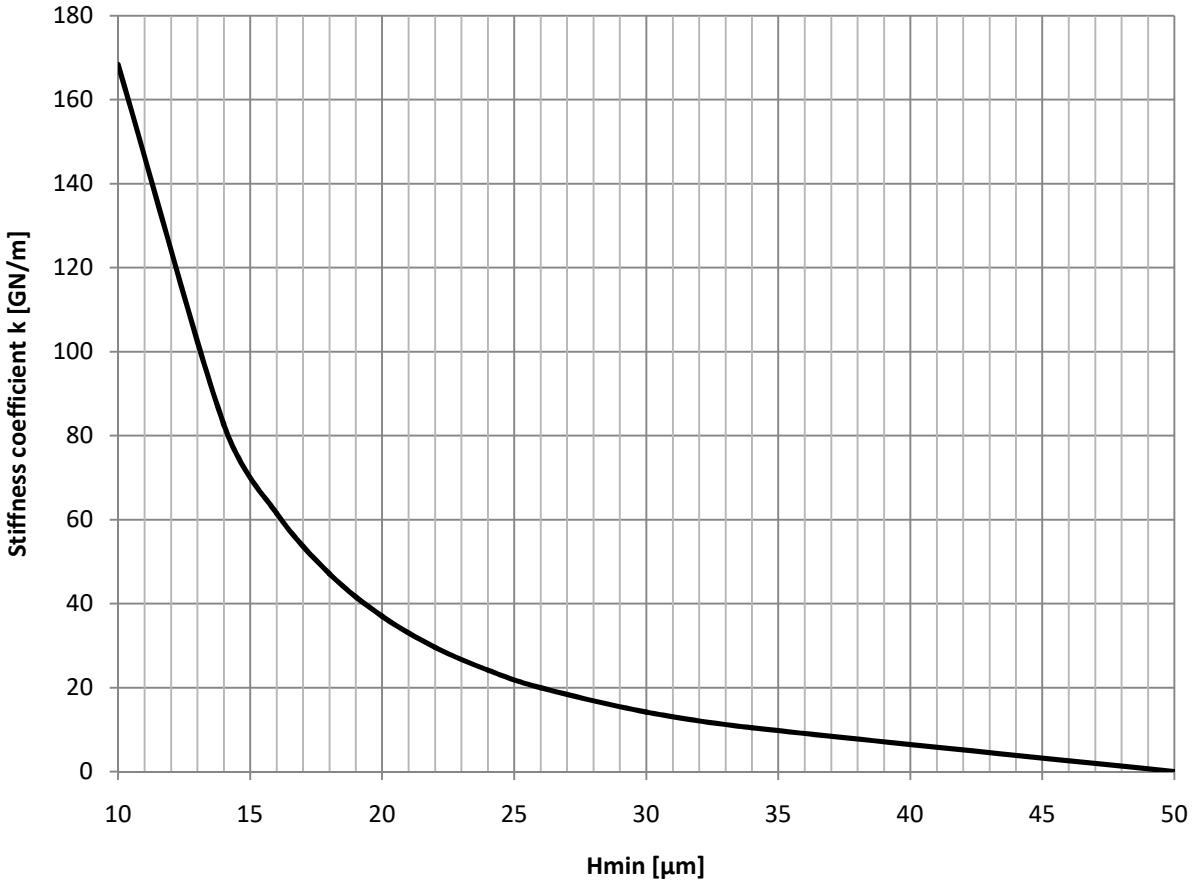

FIGURE 5.11: Stiffness coefficient k - Minimum film thickness H_{min}.

In order to calculate the damping coefficient according to equations (46a) and (46b) the steady state load at the final position $x \pm \Delta x$ is required. An extra set of steady state simulations have been conducted, whose results are listed in Table 5.7.

Subsequently, the damping coefficients for each acceleration value of the approaching and distancing conditions have been calculated and displayed in Fig. 5.12a and 5.12b. The damping coefficient when the rotor is approaching the pad is higher than that when it is moving away from it. The difference between the various acceleration values is slight.

TABLE 5.7: Steady load at position $x \pm \Delta x$.

H_{min} (µm)	Steady Load (N)	
	Approaching	Distancing
10	1,701.23	1,666.95
14	1,168.57	1,148.82
16	991.96	976.59
18	853.83	841.71
20	743.84	734.09
22	654.93	647.00
24	582.14	575.63
26	521.60	516.10
30	426.89	422.89
34	357.42	354.45

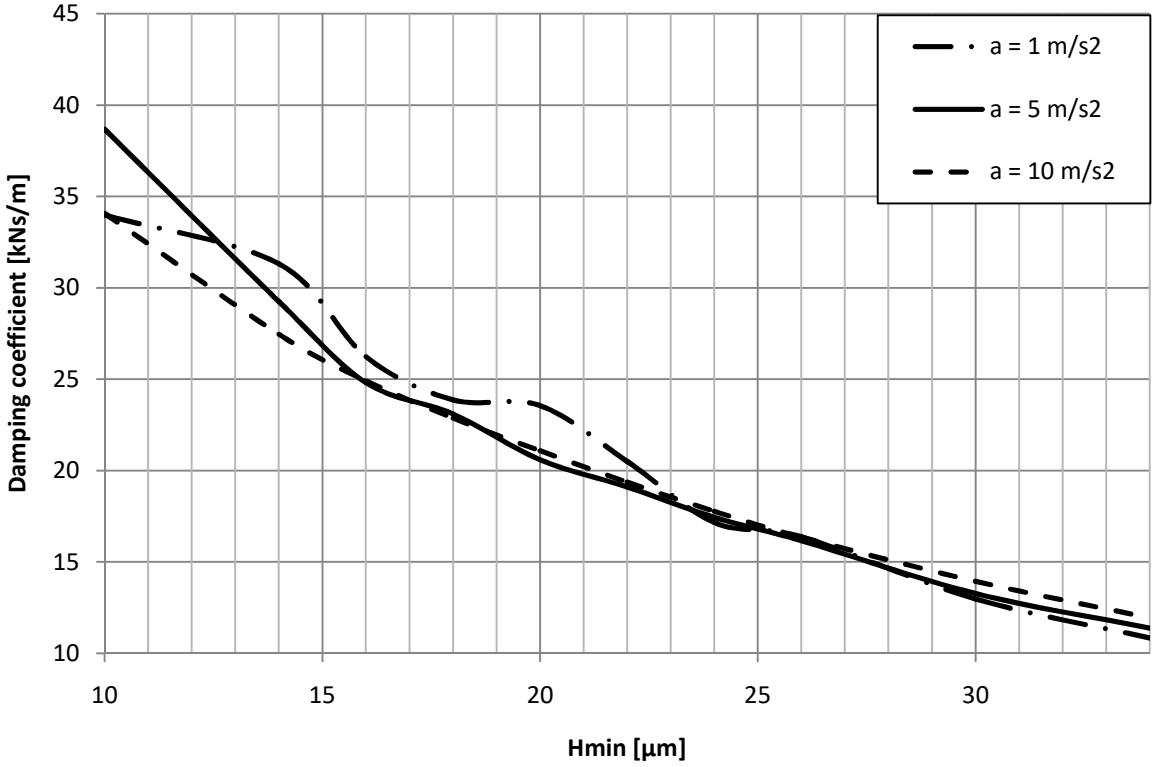

(a)

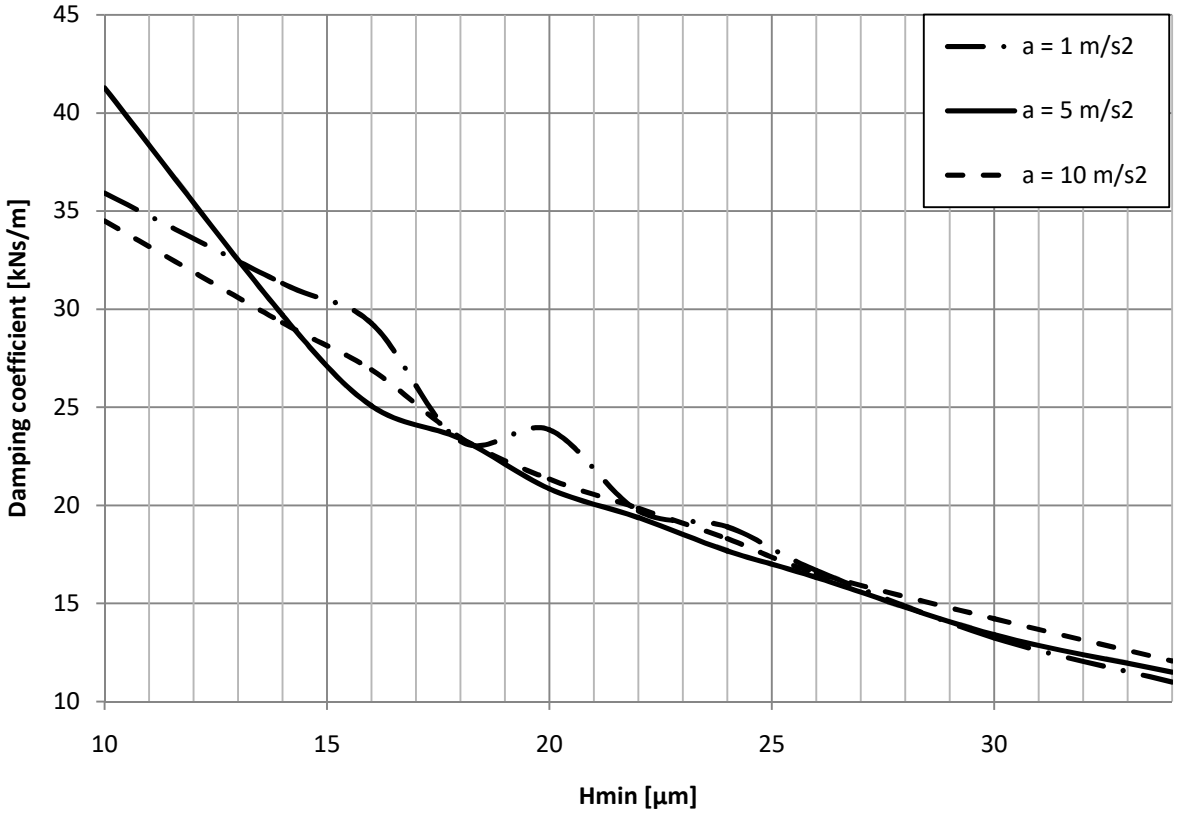

(b)

FIGURE 5.12: Damping coefficient - minimum film thickness Hmin and acceleration α: (a) distancing, (b) approaching.

Single degree of freedom results

After the calculation of the stiffness and damping coefficients the single degree of freedom model has been setup. As mentioned above, it is necessary for the stiffness coefficient to be equal to zero at the selected rest position. The rotor's displacement *x* is evaluated from the rest position and then the minimum film thickness is calculated. When the external load is zero, the single degree of freedom model should be at the rest position. If the stiffness coefficient is non-zero then a restoring force will cause the rotor to constantly move away from the pad. This inaccuracy of the stiffness coefficient does not affect the bearing's behaviour in normal conditions, since the bearing has been set at the nominal minimum film thickness before starting the transient loading.

The loading condition imposed on the model lasts a total of 40 ms. In Fig. 5.13, the transient load is displayed. During the first 10 ms, there is only the steady-state load applied to set the initial minimum film thickness condition. Subsequently, the transient loading is applied. The RMS

acceleration value is approximately 9.4 m/s^2. The maximum compression additional load reaches almost the value of 100 N.

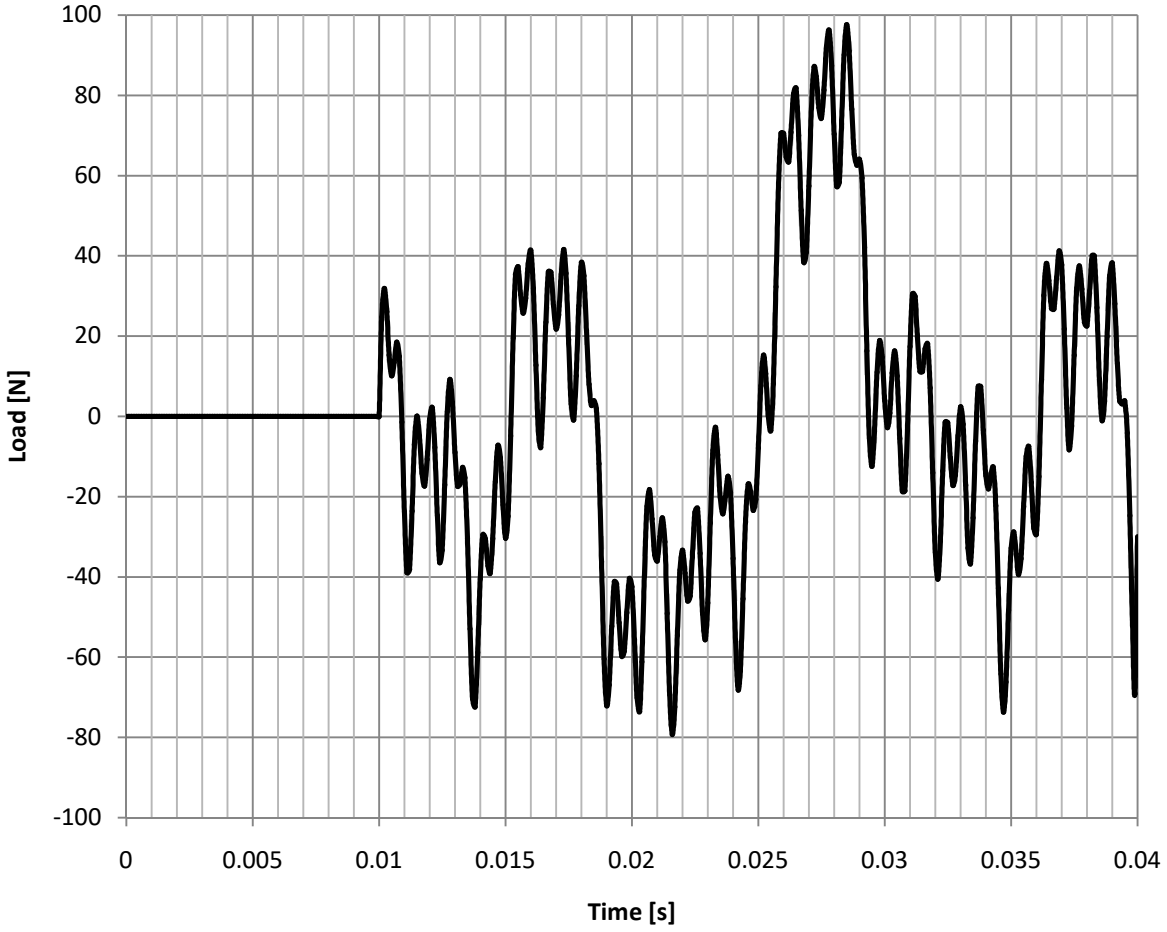

FIGURE 5.13: Single degree of freedom transient load.

The fixed step Runge-Kutta (ode4) solver was used for the solution of the differential equations with a time-step of 0.0001 s.

In the following figures, Fig. 5.14 and Fig. 5.15, the initial steady state condition –lasting 10 ms- has been ignored. Fig. 5.14 displays the variation of the minimum film thickness H_{min} and the stiffness coefficient k over time due to the transient load. Fig. 5.15 displays the variation of the rotor's velocity $\dot{x}$ and the damping coefficient c.

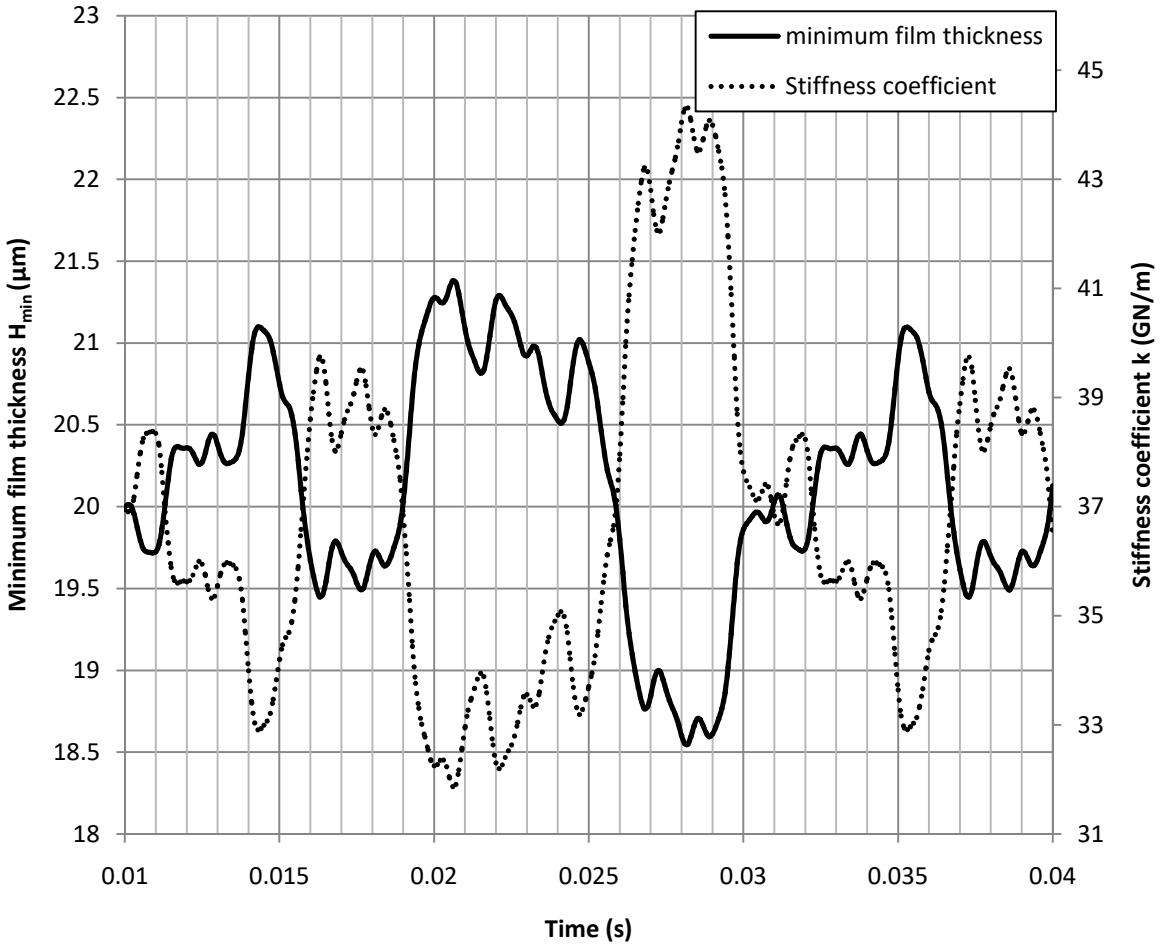

FIGURE 5.14: Minimum film thickness and stiffness coefficient variation due to the transient load.

When the load decreases, the minimum film thickness increases, causing a reduction in the stiffness and damping coefficients. The damping coefficient plotted in Fig. 5.15 is the one that has been selected depending on the direction of the rotor's motion, which has then been multiplied with the velocity to calculate the damping force.

At this point, it should be highlighted that the velocity function's frequency is higher than the minimum film thickness function's. This is due to the transient load function selected. Velocity is calculated by integrating acceleration which has the same frequency as the load. The load is composed of a sum of sinusoidals with different frequencies. When integrated, each component is multiplied by a factor of $\frac{1}{\alpha \cdot \omega}$, in which α = 0.5, 1, 2, 4, 8 and 16. Hence, the high frequency terms become less important while the amplitude of the term with α = 0.5 is enhanced. The same occurs in the case of the minimum film thickness which is calculated from the velocity derivative.

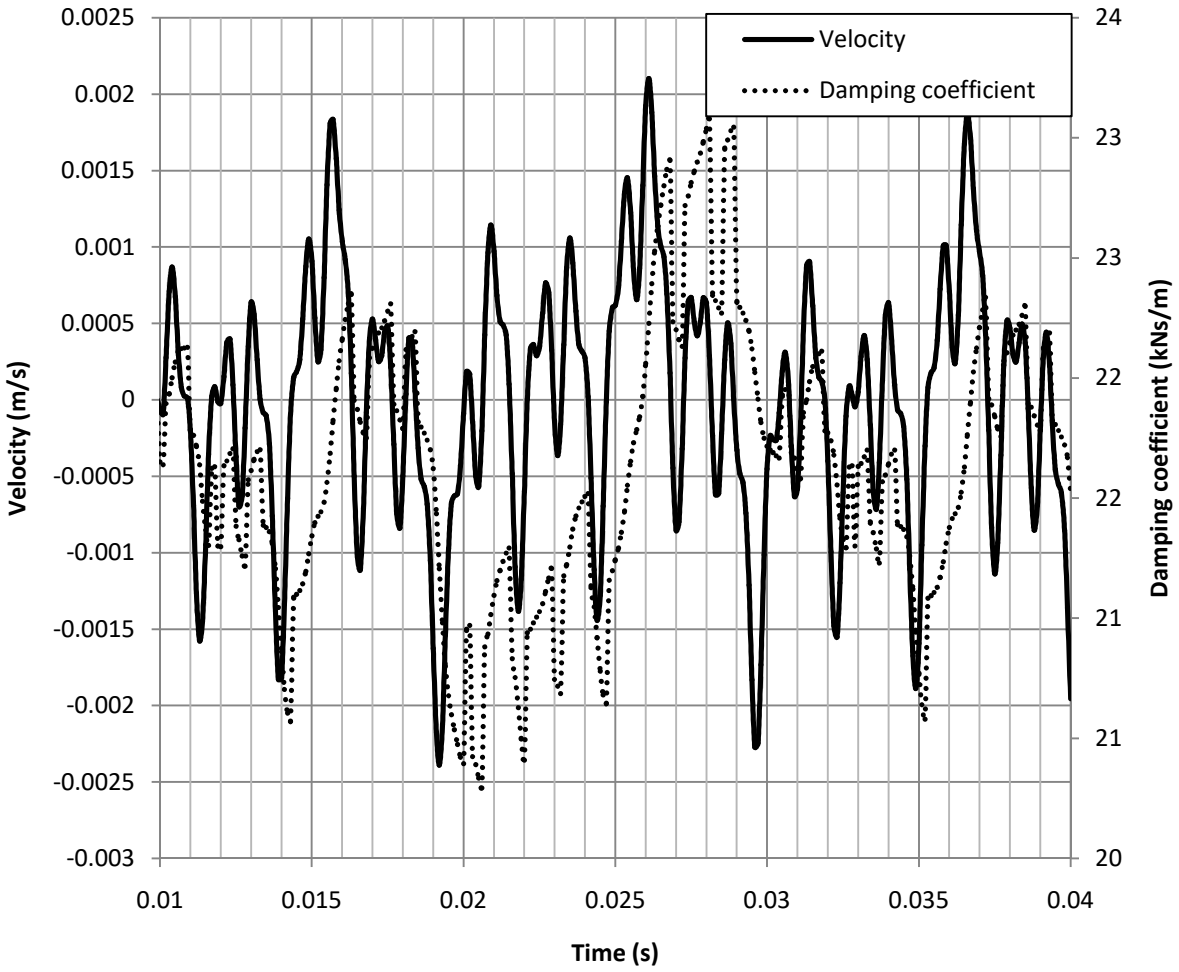

FIGURE 5.15: Velocity and damping coefficient variation due to the transient load.

Fig. 5.16, below, displays the rotor's free body diagram at four separate time-steps representing four different cases. On the top two diagrams, the rotor is approaching the pad while on the bottom two, it is moving away. The two on the left have positive acceleration, while the two on the right, negative.

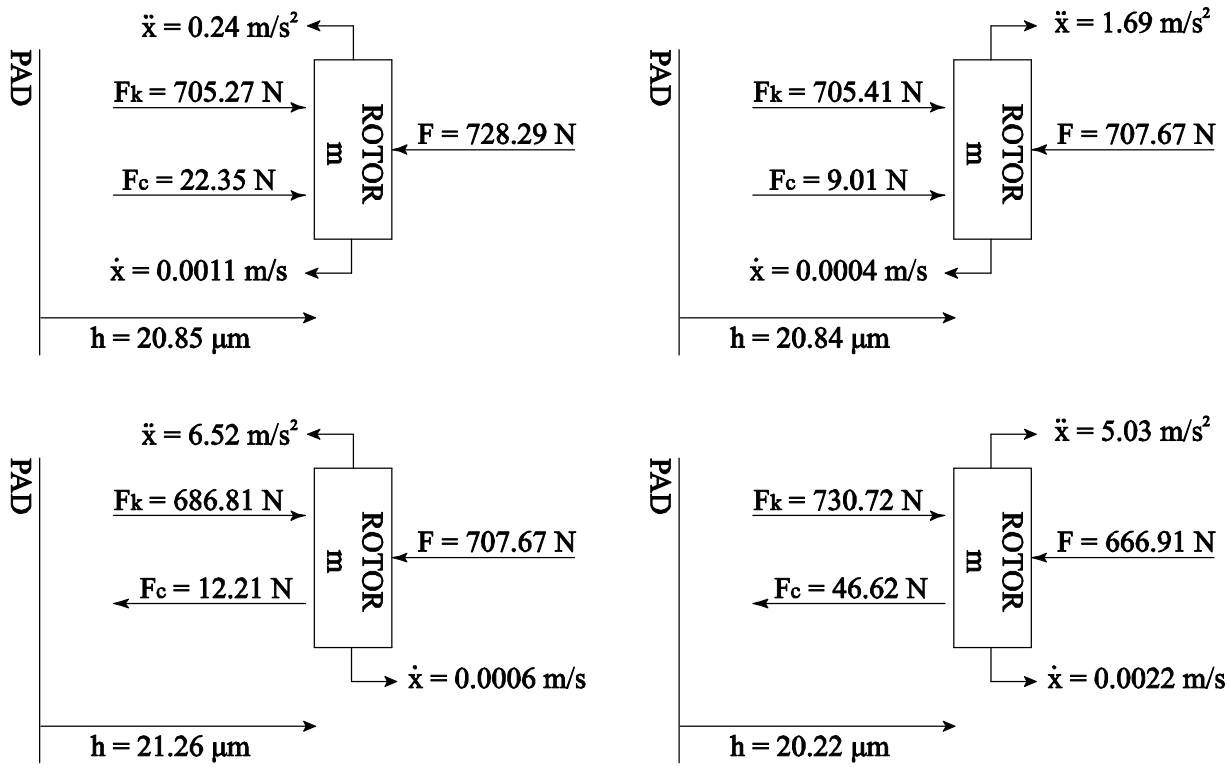

FIGURE 5.16: Free body diagram.

To evaluate the results a final transient CFD analysis has been conducted. The displacement that resulted from the single degree of freedom modeling has been imputed as a forced displacement to the rotor on a transient CFD simulation. The resulting force history has been compared to the initial transient force used for the single degree of freedom calculation in Fig. 5.17. The results from the ANSYS transient analysis indicate good agreement with the load set in the single degree of freedom model initially. There is a slight delay which is however negligible. The most important difference is that the resultant force does not capture the high frequency variations imposed in the initial load.

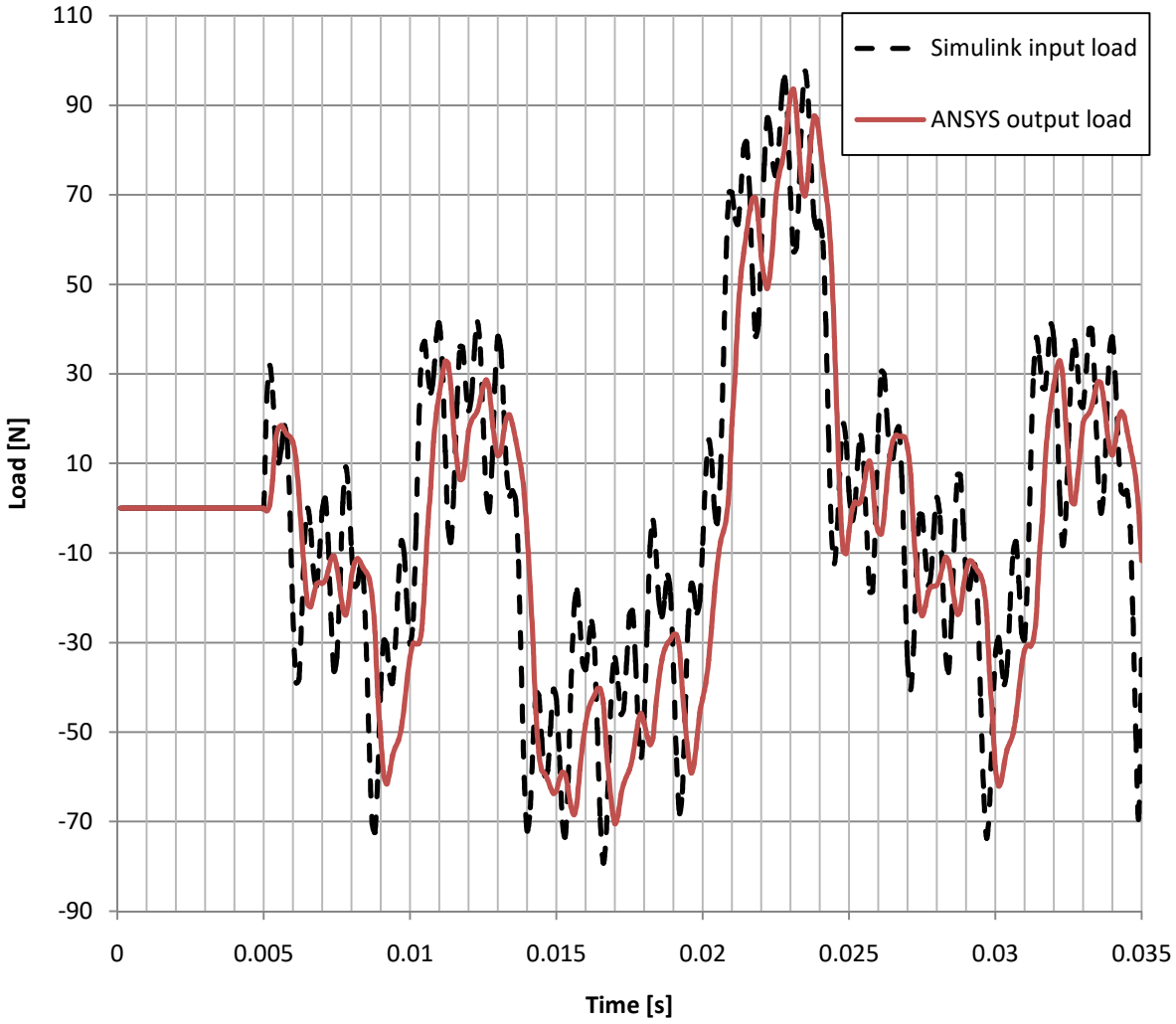

FIGURE 5.17: Simulink - ANSYS load comparison.

6. Conclusion – Future work

Conclusion

Taking everything into account, in the present work, the dynamic characteristics of a tapered-land fluid film thrust bearing have been defined permitting the prediction of the bearing's response when loaded with a transient force.

Initially, parametric analysis has been conducted to define the tapered-land's geometric characteristics. The analysis examined which couple of taper extent and inclination led to the optimum bearing at a specific minimum film thickness, which was decided by looking at the load to friction torque ratio. Increasing the inclination, increases the taper opening area, thus, allowing greater lubricant's flow in the bearing. Increased flow translates into increased maximum pressure. However, after the taper inclination optimum value the load appears to decrease. On the other hand, friction torque keeps increasing as the taper inclination increases, leading to the decline of the ratio.

Having determined the optimum geometry for the bearing, the stiffness and damping coefficients have been calculated through a thermo-hydrodynamic (THD) computational fluid dynamics (CFD) analysis which solved the Navier-Stokes equations. The analysis started with a steady-state simulation, in which the rotor has been set at a specific minimum film thickness. Subsequently, a perturbation of the minimum film thickness has been imposed. The rotor's perturbation consisted in a constant acceleration motion to either approach or move away from the pad. Three acceleration values have been examined according to the expectations. A new steady-state simulation has been conducted at the final perturbation position. The results of the analysis yielded a map for each coefficient.

After the determination of the bearing's dynamic coefficients, a single degree of freedom has been utilised to predict the response of the bearing under a transient loading condition. The single degree of freedom model developed consisted in a mass supported by a non-linear couple of damper and compression only spring. The stiffness coefficient of the spring is calculated depending on the current minimum film thickness. The damping coefficient, on the other hand, is calculated for both approaching and distancing conditions as a function of the minimum film thickness. Depending on the value of the velocity, the correct set is selected and then the final value derived by interpolating over the acceleration. The transient force imposed on the system was a sum of sinusoidal wave function of different amplitudes, wave lengths and phases.

Finally, to evaluate the single degree of freedom results, the displacement derived has been set as a motion of the rotor in a new transient CFD analysis. The load function that resulted agreed with the initial loading force applied to the single degree of freedom model, validating the results.

Future work

The methodology proposed in the present work consists in an important step towards the dynamic analysis of thrust bearings. Nevertheless, many more aspects could be investigated in future work, such as the topics suggested below.

1. Temperature dependent lubricant's properties: In the present work, only viscosity was considered to be temperature dependent. However, all other properties are affected by the temperature, especially the lubricant's density, and should be considered.

2. Rotor's tilting motion: A similar procedure should be developed for the tilting motion of the rotor to examine its' behaviour

3. Other thrust bearing geometries: Different pad geometries should be analysed and compared to determine which displays the best dynamic characteristics

4. Pivoting-pad bearing: Marine thrust bearings used to support the propeller's thrust are have a pivoting pad. The methodology could be applied to such bearings to determine their behaviour. In extreme conditions, such as in cases of propeller ventilation, there may be huge thrust load differences, which could be of great interest

5. Open source CFD code: During the course of this thesis, the use of the open source CFD code OpenFOAM was investigated. While it provides the user with many capabilities, at the moment, there is no conjugate heat transfer transient solver available. In addition, there are no cavitation models that can be applied. These features could be developed in future versions or generated by users allowing this kind of computations.

Literature - References

1. A. Cameron, 1976, “Basic lubrication theory”, Ellis Horwood Limited
2. GwidonW. Stachowiak, Andrew W. Batchelor 1993, “Engineering tribology”, Butterworth-Heinemann, Elsevier
3. Frank M. White, 1999, “Fluid mechanics”, McGraw-Hills
4. Γιώργος Μπεργελές, 2012, “Υπολογιστική ρευστομηχανική”, Εκδόσεις Συμεών, Αθήνα
5. John D. Anderson Jr., 1995, “Computational fluid dynamics: The basics with applications”, McGraw-Hill
6. F. Moukalled, L. Mangani, M. Darwish, 2016, “The finite volume method in computational fluid dynamics: An advanced introduction with OpenFOAM® and Maltab®”, Springer
7. Σωκράτης Τσαγγάρης, 2015, “Μηχανική των Ρευστών: Θεωρία και ασκήσεις”, Εκδόσεις Τσώτρας, Αθήνα
8. J. S. Carlton, 1994, “Marine propellers and propulsion”, Butterworth-Heinemann, Elsevier
9. Eskild Storteig, Maurice White, 1999, “Dynamic characteristics of hydrodynamically lubricated fixed-pad thrust-bearings”, Elsevier, Vol. 232, Issue 2, pp. 250-255, DOI: 10.1016/S0043-1648(99)00153-2
10. Zhu Q., Zhang W. J., 2003, “A Preliminary Nonlinear Analysis of the Axial Transient Response of the Sector-Shaped Hydrodynamic Thrust Bearing-Rotor System”, ASME Journal of Tribology, Vol. 125, Issue 4, pp. 854-858, DOI: 10.1115/1.1575775
11. Jang, Lee, 2006, “Determination of the dynamic coefficients of the coupled journal and thrust bearings by the perturbation method”, Tribology Letters, Vol. 22, Issue 3, pp. 239-246, DOI: 10.1007/s11249-006-9087-7
12. D. V. Srikanth, K. K. Chaturvedi, A. C. K. Reddy, 2009, “Modelling of Large Tilting Pad Thrust Bearing Stiffness and Damping Coefficients”, Tribology in Industry, Vol. 31, Issue 3&4, pp. 23-27
13. Papadopoulos, Nikolakopoulos, Kaiktsis, 2012, “Characterisation of stiffness and damping in textured sector pad micro thrust bearings using computational fluid dynamics”, ASME Journal of Engineering for Gas Turbines and Power, Vol. 134, Issue 11, pp. 854-858, DOI: 10.1115/1.4007320
14. Qin, Jahn, Jacobs, 2016, “Prediction of Dynamic Characteristics of Foil Thrust Bearings using CFD”, *20th Australasian Fluid Mechanics Conference,* Perth Australia, 5/12-8/12
15. Luis San Andrés, Keun Ryu, Paul Diemer, 2015, “Prediction of Gas Thrust Foil Bearing Performance for Oil-Free Automotive Turbochargers”, ASME Journal of Engineering for Gas Turbines and Power, Vol.137, Issue 3, DOI: 10.1115/1.4028389
16. Snyder, Braun, 2018, “Comparison of Perturbed Reynolds’ Equation and CFD Models for the Prediction of Dynamic Coefficients of Sliding Bearings”, MDPI Lubricants, Vol. 6, Issue 1, DOI:10.3390/lubricants6010005
17. Takenaka, K, Hayashi, T & Miyagawa, K, 2017, “Application of CFD analysis for static and dynamic characteristics of hydrodynamic journal bearing” Paper presented at the 17th

International Symposium on Transport Phenomena and Dynamics of Rotating Machinery, ISROMAC 2017, Maui, United States, 16/12 - 21/12
18. Qiang Li, Suo Zhang, Long Ma, Weiwei Xu, Shuiying Zheng, 2017, “Stiffness and damping coefficients for journal bearing using the 3D transient flow calculation”, Journal of Mechanical Science and Technology, Vol. 31, Issue 5, pp. 2083-2091
19. L. C. Vieira, K. L. Cavalca, 2012, “Analysis of the influence of force and moment dynamic coefficients on lubricated thrust bearings”, 10th International Conference on Vibrations in Rotating Machinery, 11/09/2012 - 13/09/2012, pp. 557-566
20. Fouflias D., Charitopoulos A., Papadopoulos C., Kaiktsis L., Fillon M., 2014, Charitopoulos, “Performance comparison between textured, pocket, and tapered-land sector-pad thrust bearings using computational fluid dynamics thermohydrodynamic analysis”, Proceedings of the Institution of Mechanical Engineers, Part J: Journal of Engineering Tribology, Vol. 229, Issue 4, pp. 376-397, DOI: 10.1177/1350650114550346
21. Charitopoulos, Visser, Eling, Papadopoulos, 2018, “Design optimization of an automotive turbocharger thrust bearing using a CFD-based THD computational approach”, Lubricants 2018, Vol. 6, Issue 1, DOI: 10.3390/lubricants6010021
22. Fouflias, Charitopoulos, Papadopoulos, Kaiktsis, 2017, “Thermodynamic analysis and tribological optimisation of a curved pocket thrust bearing”, Tribology International, Vol 110, pp. 291-306, DOI: 10.1016/j.triboint.2017.02.012